

Cortical pyramidal and parvalbumin cells exhibit distinct spatiotemporal extracellular electric potentials

<https://doi.org/10.1523/ENEURO.0265-22.2022>

Cite as: eNeuro 2022; 10.1523/ENEURO.0265-22.2022

Received: 2 July 2022

Revised: 18 October 2022

Accepted: 7 November 2022

This Early Release article has been peer-reviewed and accepted, but has not been through the composition and copyediting processes. The final version may differ slightly in style or formatting and will contain links to any extended data.

Alerts: Sign up at www.eneuro.org/alerts to receive customized email alerts when the fully formatted version of this article is published.

Copyright © 2022 Sukman and Stark

This is an open-access article distributed under the terms of the Creative Commons Attribution 4.0 International license, which permits unrestricted use, distribution and reproduction in any medium provided that the original work is properly attributed.

Cortical pyramidal and parvalbumin cells exhibit distinct spatiotemporal extracellular electric potentials

Lior J. Sukman, Eran Stark

Sagol School of Neuroscience and Department of Physiology and Pharmacology, Sackler Faculty of Medicine, Tel Aviv University, 6997801, Israel

Corresponding author: Eran Stark, eranstark@tauex.tau.ac.il

Abbreviated title: Spatiotemporal extracellular potentials

<i>Number of figures:</i>	6
<i>Number of tables:</i>	4
<i>Number of multimedia and 3D models:</i>	0
<i>Number of words in Abstract:</i>	222
<i>Number of words in Significance Statement:</i>	93
<i>Number of words in Introduction:</i>	654
<i>Number of words in Discussion:</i>	1816

Acknowledgments: This work was supported by the United States-Israel Binational Science Foundation (BSF) 2015577; by the European Research Council 679253; by the Rosetrees Trust A1576; by the Canadian Institutes of Health Research (CIHR), the International Development Research Centre (IDRC), the Israel Science Foundation (ISF) and the Azrieli Foundation 2558/18; and by the Zimin Institute. We thank Ronny Eichler and Lisa Roux for help collecting data, and Michal Altmark, Gil Davidovich, and David Gertskin for contributions during early steps of the project. We are grateful to Lidor Spivak and Amir Levi for constructive comments.

Financial interests or conflict of interests: The authors declare no competing financial interests.

Author contributions: E.S. designed research; L.J.S. and E.S. performed research; L.J.S. and E.S. contributed unpublished reagents/analytic tools; L.J.S. and E.S. analyzed data; L.J.S. and E.S. wrote the first draft of the paper; L.J.S. and E.S. edited the paper; L.J.S. and E.S. wrote the paper.

Abstract

Brain circuits are composed of diverse cell types with distinct morphologies, connections, and distribution of ion channels. Modeling suggests that the spatial distribution of the extracellular voltage during a spike depends on cellular morphology, connectivity, and identity. However, experimental evidence from the intact brain is lacking. Here, we combined high-density recordings from hippocampal region CA1 and neocortex of freely-moving mice with optogenetic tagging of parvalbumin-immunoreactive (PV) cells. We used ground truth tagging of the recorded pyramidal cells (PYR) and PV cells to construct binary classification models. Features derived from single-channel waveforms or from spike-timing alone allowed near-perfect classification of PYR and PV cells. To determine whether there is unique information in the spatial distribution of the extracellular potentials, we removed all single-channel waveform information from the multi-channel waveforms using an event-based delta transformation. We found that spatiotemporal features derived from the transformed waveforms yield accurate classification. The extracellular analogue of the spatial distribution of the initial depolarization phase provided the highest contribution to the spatial-based prediction. Compared to PV cell spikes, PYR spikes exhibited higher spatial synchrony at the beginning of the extracellular spike and lower synchrony at the trough. The successful classification of PYR and PV cells based on purely spatial features provides direct experimental evidence that spikes of distinct cell types are associated with distinct spatial distributions of extracellular potentials.

Significance statement

It is not clear if and how neuronal morphology, cell type, and synaptic inputs are mapped to the spatial distribution of the extracellular voltage during spikes. Here we show that spatial information alone allows accurate differentiation between pyramidal cells and parvalbumin-immunoreactive cells in

24 neocortex and hippocampus of freely-moving mice. The ability to distinguish cell types based on
25 spatiotemporal properties of extracellular potentials suggests that neurons with distinct morphology,
26 connectivity, and ion channel distributions create unique and learnable extracellular patterns. Further
27 research may reveal whether unique spatial information is characteristic of other cell types.

Introduction

Brain circuits are composed of different cell types with distinct roles in neuronal network dynamics (Tremblay et al., 2016; Tasic et al., 2018). Since the days of Brodmann (1909) and Ramón y Cajal (1909), it has been recognized that neurons in different brain regions, nuclei, and layers may have different morphologies (McKay and Turner, 2005; Ascoli et al., 2007; Clasca et al., 2012; Jones, 2012; Fujishima et al., 2018). Within a brain region, neurons that vary in the type of output (e.g., excitatory, inhibitory) and postsynaptic targets (e.g., somatic, dendritic, or axonal) exhibit distinct morphology (Markram et al., 2004; Klausberger and Somogyi, 2008; Kepecs and Fishell, 2014). Histological and in vitro studies showed that the size, form, and orientation of the soma, the dendritic tree, and the axonal arbor, all vary between cells that express different genes and neurochemical markers (Monyer and Markram, 2004; Zeisel et al., 2015; Zeng and Sanes, 2017).

In behaving animals, extracellular recording techniques allow simultaneous recording of electrical potentials generated by multiple neurons and sampling every neuron at several spatial locations (Buzsáki, 2004; Shobe et al., 2015; Jun et al., 2017; Hong and Lieber, 2019; Steinmetz et al., 2021). Multi-site recordings with well-defined electrode geometry open the door to blind cell type classification based on electrophysiological properties. The relation between morphology (structure) and neuronal cell type (function) is well established in vitro and using post-mortem immunohistology (McCormick et al., 1985; Freund and Buzsáki, 1996; Somogyi and Klausberger, 2005). Extensive modeling work has been dedicated to understand the relationship between the spatial distribution of extracellular electrical potentials resulting from spikes and neuronal morphology (Rall, 1962; Gold et al., 2009; Einevoll et al., 2013). However, the relationship between the spatial distribution of extracellular electrical potentials and neuronal cell types in the intact brain remains unexplored.

To determine whether spikes of different cell types give rise to distinct distributions of extracellular potentials, we focus here on pyramidal cells (PYR) and parvalbumin-immunoreactive (PV) cells in

neocortex and hippocampal region CA1. PYR have pyramid-shaped somata and vertically-oriented, apical and basal (polar) dendritic trees (Spruston, 2008). In contrast, PV (mainly basket) cells have less polarized dendritic trees, and axonal arbors that extend horizontally (Maccaferri et al., 2000; Pawelzik et al., 2002; Ganter et al., 2004). Furthermore, PYR and PV cells exhibit distinct spatial profiles of ion channels. While similar somato-dendritic gradients are observed for Na^+ channels, K^+ channels exhibit a steeper decreasing gradient along dendrites farther from the soma in PYR, compared to PV cells (Magee and Johnston, 1995; Johnston et al., 2000; Hu et al., 2010). To go beyond descriptive structure-function relations, we hypothesized that PYR and PV cells could be classified based solely on spatial information acquired from freely-moving mice using high-density probes. Previously, classification of PYR and interneurons in neocortex and hippocampus was based on waveform features (Henze et al., 2002; Barthó et al., 2004; Cardin et al., 2009; Stark et al., 2013; Mendoza et al., 2016; Yu et al., 2019), firing patterns (Taira and Georgopoulos, 1993; Kobayashi et al., 2019; Troullinou et al., 2020), or combinations thereof (Csicsvari et al., 1998; Frank et al., 2001; Viskontas et al., 2007). However, cell type classification based on spatial features per se was never attempted.

Here, we used connectivity-based and optical tagging to establish a dataset of labeled PYR and PV cells from neocortex and CA1 of freely-moving mice. To tune the classification procedure and determine baseline performance, we first created classification models that used features based on single-channel waveforms or on spike-timing. Using a chunking-based data augmentation method, the models achieve near-perfect performance. Next, we devised an event-based delta-transformation method to conserve only purely spatial information, and derived spatial features from the multi-channel recordings. Models trained on spatial features derived from the transformed waveforms yield accurate classification. The findings suggest that differences between PYR and PV neuronal morphology, connectivity, and ion channel distributions are reflected in the extracellular potentials in a consistent manner.

Materials and Methods

Experimental design

The dataset used in this study has been previously analyzed (Stark et al., 2013).

Experimental animals

Seven PV::ChR2 male mice, generated by crossing homozygous male Ai32 mice (#012569, Jackson labs) with homozygous female PV-Cre mice (#008069, Jackson Labs), were used for chronic recordings. The animals and data were used for the work by Stark et al., 2013. All animal handling procedures were approved by the Rutgers University and New York University Animal Care and Facilities committees.

Probes and surgery

Every animal was implanted with a four-shank diode probe as previously described (Stark et al., 2012). Probes were constructed by coupling 470 nm blue LEDs (LB P4SG, Osram; 2 mm diameter) to 50 μ m multi-mode optical fibers and attaching every diode-fiber assembly to a single shank of a 32-site/four-shank silicon probe (Buzsaki32, NeuroNexus). Fiber tips were located ~50 μ m above the top recording site. Probes were implanted in the right hemisphere at PA -1.6/ML 1.1 mm under isoflurane anesthesia. During surgery, the probes were lowered to a depth of 0.4-0.7 mm.

Recordings and photostimulation

After allowing the animals to recover for at least 48 hours, recordings were initiated. Recordings were carried out in the home cage during spontaneous behavior. Mice were tethered by one ultralight cable for multi-channel neuronal recordings and a second cable for multi-channel optical stimulation.

Recordings were conducted as the probe was moved gradually from the neocortex to the CA1 pyramidal cell layer. At each location in the brain, neuronal activity was inspected for spontaneous spiking activity, and if encountered, a baseline period of at least 15 minutes was recorded followed by photostimulation (peak driving current, 60 mA; mean \pm SD peak light power: 35 \pm 7 μ W; 50-70 ms pulses). Signals were generated by custom code written in MATLAB (MathWorks), converted by a digital signal processor (RX5 and/or RX6, TDT) to voltage signals, and fed into a linear 16-channel current source. After each session, the probe was either left in place or moved (35-70 μ m steps), and the brain was allowed to settle overnight.

Spike sorting and ground truth labels

During recordings, neural activity was filtered (1-5,000 Hz), amplified (x20 by Plexon headstages and x50 by an RC Electronics system), and digitized (16 bits, 20 kHz) on a 128-channel DataMax recording system (RC Electronics). Applied currents were recorded by the DataMax system. Offline, spike waveforms (32 samples per channel) were extracted from the wide-band records, detrended, and sorted into single units automatically (Harris et al., 2000), followed by manual adjustment. Only well-isolated units (amplitude >50 μ V; L-ratio <0.05, Schmitzer-Torbert et al., 2005; ISI index <0.2, Fee et al., 1996) were considered. A total of 199 neocortical and 781 CA1 units conformed to these criteria.

For connectivity-based tagging, we tagged units that participated as a reference in a cross-correlation histogram (CCH) that exhibited a significant (p <0.001, Bonferroni-corrected Poisson test) peak in the monosynaptic time range (0 to 5 ms) as excitatory cells (424/980 units). Units that exhibited a significant trough in the monosynaptic time range were tagged as inhibitory (21/980 units). For optogenetic-based tagging, units that exhibited a significant (p <0.001, Poisson test) increase in spiking rate during 50-70 ms DC pulses given on the recording shank were tagged as optically-activated cells; 98/980 (10%) units conformed to the criterion. Next, we labeled units based on the three tags. Units tagged exclusively as

excitatory were labeled as PYR (420 units), whereas units that were optically-activated or inhibitory (but not excitatory) were labeled as PV cells (102 units). The remaining units (458/980, 47%) were not labelled and were discarded from the dataset. Ten of the labeled units (nine PYR, one PV) were recorded using seven instead of eight channels and were therefore discarded as well, yielding a final dataset that included 512 tagged units (411 PYR, 101 PV; **Fig. 1**). Of the 101 units referred to as “PV cells”, 93 were optically activated (92%), 13 were both optically activated and inhibitory, and eight units were only inhibitory. Spike width, firing rate, and bursting behavior were similar for the inhibitory and the optically tagged PV cells. Thus, the eight inhibitory-tagged PV-like cells were grouped with the 93 optically-activated cells, and the entire group was denoted as PV. A majority of the units (449/512) were recorded from CA1. The median [inter-quartile interval, IQR] number of spikes per unit was 8,368 [4,494 16,929] for PYR, and 66,850 [13,031 174,802] for PV cells.

Classification

Feature extraction

The shape and timing of the recorded spikes were used to extract a total of 34 features. We derived features of three modalities: waveform-based features, derived from a single channel (n=8); spike-timing features, ignoring the spike waveform (n=8); and spatial features, derived from the multi-channel waveforms (n=18). All features were based exclusively on spontaneous events that occurred in the lack of any light stimuli. For every spike, the waveform was extracted for 32 samples (1.6 ms) on every channel of the recording shank. The limited duration of the spikes places an upper bound on the classification performance of waveform-based and spatial models. For every channel separately, the waveform was averaged over spikes, and the mean waveform was calculated and upsampled eight-fold using Fourier interpolation to increase the temporal resolution. Since the average and the Fourier transform are linear operators, the order of the two steps does not affect the outcome.

Single-channel feature extraction

For the waveform-based features, the channel with the largest trough-to-peak (TTP) magnitude was denoted as the “main” channel. The waveform in the main channel was scaled by dividing all values by the minimal value (i.e., at the trough). Scaling was done to remove information about the sampling process, e.g., electrode impedance and neuron-electrode distance. When the absolute value at the trough was smaller than at the peak, waveforms were inverted (multiplied by -1). The outcome is a 256-element vector limited to the [-1, 1] range, with at least one value at -1. To provide a rich description of the waveform, a total of $n=8$ waveform-based features were extracted from the main channel (**Fig. 2; Table 1**): four from the waveform itself, one from the first temporal derivative, and three from the second temporal derivative. For every feature, we compared the distribution of values between all available PYR ($n=411$) and PV cells ($n=101$) and calculated effect sizes. The specific measure of effect size used was the nonparametric estimator for common-language effect size (A_w ; Ruscio, 2008) which exhibits a smaller bias compared to alternatives (Li, 2016). A_w estimates the probability that a random sample from one distribution is larger than a random sample from a second distribution. Disregarding the direction of the effect, A_w is thus limited to the 0.5 to 1 range, taking a value of 0.5 when the two distributions are fully intermixed, and 1 when the two distributions do not overlap at all. All eight features (100%) exhibited a consistent difference ($0.64 \leq A_w \leq 0.98$; $p < 0.05$, U -test; **Table 1**). Thus, all waveform-based features are potentially useful for classification.

The addition of a redundant feature would contribute no additional information to the classification process. To estimate relations between features, we first computed rank (Spearman’s) correlation coefficients (CCs) between every possible pair of waveform-based features (Extended Data **Fig. 2-1A**). To go beyond monotonic relations, we estimated mutual information (MI) between distributions of pairs of features (Timme and Lapish, 2018). If a feature had less than ten unique values, the feature was

considered naturally discrete; only the *SPD-Count* feature (see *Spatial feature extraction* below) was naturally discrete. The use of ten bins limits the maximal information to $\log_2 10 = 3.3$ bits. Deviation from chance level was determined using a permutation test, creating a null distribution based on 5,000 iterations of shuffled pairs and evaluating the tail of the null distribution above the observed MI. We found that some features were only weakly correlated with others (e.g., the *Break-measure*, median [IQR] absolute CC 0.19 [0.076 0.24]), suggesting that independent information could be gleaned by using the feature. Alternatively, a weakly-correlated feature may be dominated by noise. However, the possibility is unlikely since the *Break-measure* differed for the PYR and PV groups ($A_w = 0.64$; $p = 7.85 \times 10^{-6}$, *U*-test; **Table 1**). Other features were more strongly correlated with the host of other features (e.g., full-width at half-maximum [*FWHM*]: 0.81 [0.45 0.87]; *Smile-cry*: 0.76 [0.33 0.91]). Since a small number of samples limits the power of standard statistical tests (e.g., the Mann-Whitney *U*-test), when comparing CCs between two groups within a modality we applied a permutation test. We compared a statistic, defined as the difference between the medians of the two groups of CCs, to the 95th percentile of a null distribution created by shuffling the CCs between the groups, and calculating the statistic 1,000 times. We did not observe stronger absolute CCs within families: the absolute intra-family correlation was 0.37 [0.14 0.62], whereas the absolute inter-family CC was 0.47 [0.24 0.79] ($p > 0.05$, permutation test). Quantifying the interrelations between waveform-based features using MI yielded similar results. The median [IQR] MI between waveform-based feature distributions was 0.658 [0.292 0.955] bits, and the rank correlation coefficient between the MI and CCs was 0.816 ($p = 0.001$, permutation test; Extended Data **Fig. 2-1B**, inset). The bulk of the variance in the MI ($R^2 = 0.67$) could be explained by pairwise rank correlations, suggesting that interrelations between feature pairs are largely monotonic. Thus, based on the feature redundancy analysis, partitioning into families may have only semantic value, and all derived features may contribute to classification.

Spike-timing features

For the features based on spike-timing, the autocorrelation histogram (ACH) was calculated for every unit over a range of $\pm 1,000$ ms using a bin size of 0.5 ms. The ACH depends only on the timing of the spikes and is agnostic to the spike waveforms. The ACH was upsampled eight-fold using polyphase filtering to increase the temporal resolution. The ACH is an even function, but edge effects necessarily cause asymmetry in any practical implementation. To obtain an ACH (0-1,000 ms) free from edge effects, the value in every positive time bin was averaged with its negative homolog. A total of $n=8$ spike-timing features were derived (**Fig. 2; Table 2**). Three of the features were high-frequency features, derived from the short-term ACH (up to 50 ms). Two were low-frequency features, derived from the long-term ACH (50-1,000 ms). The last three were wide-band features: two were derived from the complete ACH (0-1,000 ms), and one was derived from the entire recording. For every feature, we compared the values derived for the PYR and PV cells. All eight features (100%) exhibited a consistent difference between PYR and PV cells ($p < 0.05$, U -test; **Table 2**). Thus, spike-timing features may be useful for classification.

To quantify interrelations, we computed CCs and MI between spike-timing features extracted from the complete spike trains (Extended Data **Fig. 2-2**). The high-frequency features exhibited high within-family absolute correlations (0.85 [0.83 0.88]), whereas lower absolute correlation values were observed between the other features (low-frequency and wide-band families together: 0.26 [0.24 0.70]; $p=0.098$, permutation test; Extended Data **Fig. 2-2A**). In contrast to the waveform-based feature families, intra-family absolute correlations (0.81 [0.49 0.83]) were higher than inter-family absolute correlations (0.50 [0.40 0.61], $p=0.012$, permutation test). MI between pairs of spike-timing features yielded similar results to the pairwise correlations. The median [IQR] MI between spike-timing features was 0.469 [0.283 0.701] bits, and the rank correlation coefficient between MI and CCs was 0.967 ($p=0.001$, permutation test; $R^2=0.93$; Extended Data **Fig. 2-2B**, inset). The fact that almost all variance of the MI values is

explained by pairwise correlations suggests that the interrelations between the pairs of features are largely monotonic. The correlations between high-frequency features, namely *Uniform-distance*, D_{KL} -*Short*, and *Rise-time* suggest that the features provide redundant information. Thus, a small number of spike-timing features may suffice for classification.

Spatial feature extraction

For extracting purely spatial features, an event-based delta transformation was first applied to the mean upsampled waveform of every channel to remove all waveform-based information (**Fig. 3A**). (1) First, positive spikes were inverted as done for the waveform-based process. (2) Next, three events were defined. One event was the time of maximal negativity (NEG). For the additional two events, the median over all the channels was calculated. The second event was the first median crossing (FMC), the first time point before the maximal negativity of the channel in which the global median was crossed. The third event was the second median crossing (SMC), the first time point after the maximal negativity of the channel in which the global median was crossed. Every event was detected on every channel, yielding a total of 24 points. (3) Third, the waveform was replaced by a delta-like function that took the value of the maximal negativity of the channel at the singular event time point and zeroes everywhere else. The delta-like functions were scaled by the absolute value of the global minimum over all channels, effectively removing all waveform-based information from every single channel. However, waveform-based information may still be available when using multiple events together (e.g., FMC, NEG, and SMC). (4) To remove all waveform-based information, the delta functions were shifted together to centralize (shift to the 129th sample) the time of the event on the main channel. The process transforms the waveform in the main channel to be nearly identical for all units (**Fig. 3B**). Residual variability in the time of the trough may remain if the channel with maximal magnitude of the TTP and the channel with the maximal negativity are not the same.

Overall, $n=18$ features were extracted from the transformed waveforms (**Table 3**) associated with the three events, quantifying three dimensions: time-based, graph-based, and value-based. (1) In the time-based dimension, only the timing of the events was considered (e.g., the standard deviation [SD] of the FMC: *FMC-Time-lag-SD*; **Fig. 3D**). Channels for which the magnitude of the TTP (prior to delta transformation) did not pass an arbitrary threshold of 25% of the maximal magnitude of the TTP over all channels were ignored (**Fig. 3D**, gray). A median [IQR] of 4 [3 5] PYR channels and 3 [2 5] PV cell channels were removed. (2) The graph-based dimension included both event timing and the physical locations of the recording electrodes on the probe. An event graph was generated based on a specific event, with a node for each channel (e.g., *FMC-Average-weight*; **Fig. 3E**). Only channels for which the magnitude of the TTP passed the 25% threshold were considered. Directed edges connected every two non-overlapping events, with a weight representing “transmission speed”: the Euclidean distance between the electrodes, divided by the time difference between the events. (3) The value-based dimension (spatial dispersion [SPD]) ignored timing information and considered the scaled maximal negativity values on every channel, based on the global maximal negativity (e.g., *SPD-Count*; **Fig. 3F**). We found that 10/18 (56%) of the spatial features exhibited differences between PYR and PV cells ($p<0.05$, U -test). Although some features do not show consistent differences between the two cell types, classification may benefit from the features due to, for instance, distinct second-order statistics.

To estimate feature redundancy due to high correlations, we computed the CCs between the spatial features extracted from the transformed mean waveforms (Extended Data **Fig. 3-1A**). The rank correlation matrix of the spatial features showed absolute correlations (median [IQR]: 0.2 [0.1 0.33]), that were weaker than for the waveform-based features ($p=3.5\times 10^{-4}$, U -test) and for the spike-timing features ($p=1.1\times 10^{-7}$). 80% of the spatial feature pairs exhibited absolute correlations higher than zero (122/153, $p<0.05$ permutation test). Intra-family absolute correlations (0.27 [0.17 0.42]) were higher than inter-family correlations (0.17 [0.08 0.29], $p=0.006$, permutation test). The median [IQR] MI

between spatial-based feature distributions was 0.19 [0.155 0.266] bits, and the rank correlation coefficient between MI and CCs was 0.84 ($p=0.001$, permutation test; $R^2=0.706$; Extended Data Fig. 3-1B). Since the correlation and the MI analysis agreed, the relatively weak correlations between spatial features may result from large amounts of noise in every feature. Alternatively, the features may provide independent information, useful for classification.

Classification procedure

The classification model was chosen to be random forests (Breiman, 1996, 2001) due to the relative simplicity. Furthermore, several methods are available for understanding the determinants of a specific random forest model prediction (e.g., Archer and Kimes, 2008). To achieve good estimation of model performance, a nested cross-validation procedure was applied (Varma and Simon, 2006; Krstajic et al., 2014). For every modality (waveform, spike-timing, and spatial) the training procedure was repeated $n=50$ times. In every iteration, data were first partitioned in an approximate 80:20 ratio into training and test sets in a stratified fashion. Thus, the training set always included 328 PYR and 80 PV cells, and the test set included 83 PYR and 21 PV cells; only the identity of the units changed between iterations. To handle the imbalance between the number of PYR and PV cells in the data set, the model weights that control the effect of every class on the impurity score used for training the random forest model were adjusted. Specifically, instead of assigning equal weights, class weights were set to be inversely proportional to the number of samples in every class using: total number of training set samples / (number of classes \times number of class samples in the training set). Second, a 5-fold grid search was conducted on the training set to find the best hyperparameters for the model, optimizing the area under the receiver operating characteristic (ROC) curve (AUC). The tested hyperparameters were the number of estimators, the depth of each estimator, the minimal number of samples required to split a node, and the minimal number of samples required to be at a leaf node. Other hyperparameters received default

290 values based on the implementation of the *scikit-learn* library in Python (Pedregosa et al., 2011). Third,
291 using the optimized hyperparameters, the model was trained on the entire training set. Finally, model
292 performance was evaluated using the test set.

293

294 *Performance and explainability*

295 Model performance was assessed using a metric that is robust to unbalanced data. Two types of
296 metrics exist: threshold-dependent and threshold-independent. Threshold-dependent metrics consider
297 only the binary decision: in our case, PYR or PV. Threshold-independent metrics consider the raw
298 prediction, a value between 0 and 1, and not the decision itself. Threshold-dependent metrics require
299 choosing a threshold, and thus the outcome may vary according to the chosen decision threshold. An
300 arbitrarily-chosen threshold does not necessarily reflect performance, especially when considering
301 unbalanced datasets (Sheng and Ling, 2006). The choice of a decision threshold is not trivial, and is the
302 subject of active research (e.g., Esposito et al., 2021). For these reasons, we used an established
303 threshold-independent metric, the AUC (Fawcett, 2006). The AUC reflects the relation between true
304 positives and false positives for all possible thresholds, and is hence threshold-independent as well as
305 suitable for unbalanced datasets.

306 The theoretical chance level for the AUC metric is 0.5. To determine the empirical chance level, the
307 performance of models trained on data with shuffled training-set labels was assessed. For every
308 modality (waveform, spike-timing, and spatial), the training procedure was conducted with the labels
309 shuffled only for the training set. The AUC exhibited the expected chance level behavior, yielding
310 median [IQR] values of waveform: 0.46 [0.34 0.57]; spike-timing: 0.46 [0.39 0.56]; and spatial: 0.48 [0.44
311 0.55]. Since chance level results were obtained on the test sets, further assessment of model
312 performance was carried out with respect to 0.5, the theoretical chance level.

To assess the contribution of every feature to the final classification prediction, we used Shapley additive explanations (SHAP) values (Lundberg et al., 2020). The SHAP method uses a game-theoretic approach to calculate an importance score for every feature in each sample, considering all inter-dependencies with other features. Since the predictions of random forest models range from 0 to 1, the contribution of every feature can take values from -1 to 1. For each model, we calculated and averaged the absolute contribution of every feature based on the test set, taking the median over the 50 partitions to avoid idiosyncrasies of a single arbitrary partition. Since the absolute value is taken, SHAP values are necessarily non-negative, creating a skewed distribution that does not have an expected value of zero. To calculate significance, we used a permutation test. The SHAP values for each feature were compared to the SHAP values obtained for the models trained with shuffled training-set labels. Models trained with shuffled labels represent chance level classifiers, for which the importance of every feature can be considered as the chance level baseline. To create a null distribution, we partitioned the dataset into a train and test sets 1,000 times. For every train-test partition, we shuffled the labels, trained the models as described previously, and calculated the SHAP values. Then, to calculate a p-value for every feature, we compared the original SHAP value to the 95th percentile of the null distribution.

Chunking method

Models trained on larger non-redundant datasets typically exhibit improved performance. Therefore, data augmentation approaches to synthetically increase the size of the dataset are often applied (e.g., Moreno-Barea et al., 2018). Augmentation may be implemented by adding noise or transforming the data (e.g., rotation and reflection in image classification; Mikołajczyk and Grochowski, 2018). Here, to augment the size of a given dataset, features were extracted from “chunks” that included subsets of spikes, instead of using all available spikes together. Thus, we increased variability using the natural

336 richness of the data that is otherwise flattened to a single mean waveform. The chunking process
337 increases the number of samples in the dataset, with the possible cost of increased noise.

338 A total of $n=7$ different chunk sizes were used, with 25, 50, 100, 200, 400, 800, or 1600 spikes per
339 chunk. For a given unit with N spikes and a chunk size C , the spikes were randomly split into $\lceil N/C \rceil$
340 chunks so that every chunk consisted of between C and $2C-1$ distinct spikes. Spikes were randomly
341 assigned to chunks. In a given split, all chunks consisted of the same number of spikes up to a difference
342 of a single spike. Every chunk received the label of the source unit. Due to the different numbers of
343 spikes recorded for PYR and PV cells (5,651,196 PYR spikes and 11,612,978 PV cell spikes), the balance
344 between PYR and PV samples changed compared to the original dataset (411 PYR and 101 PV cells). For
345 instance, using a chunk size of 25 spikes, the total number of PYR samples was 225,850 while the
346 number of PV samples was 464,473.

347 To determine features for every chunk separately, the waveforms were averaged over all available
348 same-channel spikes within a chunk, from which waveform and spatial features were derived. To derive
349 chunk-specific spike-timing features, the ACH was accumulated by summing over all single-spike ACHs.
350 For every spike, the single-spike ACH was based on all spikes that occurred in the -1,000 to 1,000 ms
351 time window around the reference spike. To be applicable to the chunking case, the single-spike firing
352 rate was defined as the mean of the inverse inter-spike intervals before and after the spike.

353 To provide information about the distribution of the values over chunks, several statistics were
354 extracted from the individual values of every chunk. Extracting statistics based on all the chunks of a unit
355 allows considering intra-unit variability as a feature. For every feature, the mean, SD and the 25%, 50%,
356 and 75% quantiles were extracted (referred to as "chunk statistics"). Note that extracting the mean out
357 of all the individual feature values of the chunks is not the same as not using chunking. Without
358 chunking, first all the waveforms are averaged, transformed, and then features are extracted. In
359 contrast, when using the mean over chunks, averaging happens at the end of the process (averaging the

360 waveforms within a chunk still happens at the beginning). If all steps are linear, the two processes yield
361 the same results. However, since feature extraction is not a linear operator, the mean statistic may
362 contain unique information. The specific statistics were chosen to capture the first and second moments
363 of the across-chunk distribution and for their simplicity. The chunk statistics can be expanded further to
364 capitalize on different properties of the distribution over different chunks. The five new chunk statistics
365 increased the total number of features used by the model six-fold. Notably, the chunk statistic features
366 were the same for all the chunks of a given unit.

367 When training models using chunks, the data were partitioned based on units. In the training set,
368 every chunk was considered independently (not as part of the unit). In addition, instead of performing a
369 grid search for every chunk size, the hyperparameters for all chunk sizes were chosen by a no-chunking
370 equivalent. Chunk statistics were extracted for the no-chunking dataset as well, so the number of
371 features was equal to the number of features in the chunking method. The models applying chunking
372 used the hyperparameters found using the no-chunking equivalent grid search, based on the same
373 partition of the data to training and test sets. For testing and evaluating, every chunk received an
374 independent prediction. Then, predictions were pooled over all same-unit chunks by casting a majority
375 vote, yielding a final chunk-based prediction for the unit.

376 When calculating the SHAP values for the chunking-based models, we randomly chose 1,000 samples
377 out of the test set. The procedure for computing SHAP values for chunking-based data was otherwise
378 the same as for the no-chunking data. The absolute SHAP value of every feature was summed together
379 with the values of the chunk statistics extracted from the same feature, yielding a single importance
380 value for every original feature.

381

Generalization analysis

Units in the tagged dataset were recorded from CA1 (449/512, 88%) and from neocortex. The availability of tagged data from two brain regions allows testing and quantifying inter-region generalization. Generalization was determined by the performance of models trained using recordings from one region on test data from the same region (“training region”), and from the other region (“non-trained-upon region”). To directly quantify generalization, we partitioned the full dataset into three sets for each training region. (1) A training set, containing approximately 80% of the training region units (CA1: 301 PYR, 58 PV; neocortex: 27 PYR, 23 PV); (2) a test set, containing the remaining 20% of the training region units (CA1: 76 PYR, 14 PV; neocortex: 7 PYR, 6 PV); and (3) a second test set, containing all units of the non-trained-upon region (neocortex: 34 PYR, 29 PV; CA1: 377 PYR, 72 PV). Waveform, spike-timing, and spatial models were trained on the reduced CA1 dataset with 50-, 1600-, and 25-spike chunks, respectively (found to yield the best performance for each modality on the combined dataset). Chunked data was used for the grid search: the training set was further partitioned into a “development set” containing 80% of the units and an “evaluation set” containing 20% of the units. If the development set contained more than 5,000 chunks, the grid search was conducted on a random subset of 5,000 chunks, minimizing run time while allowing an efficient search. The difference in the number of units between the CA1 and neocortical training sets leads to an inherent difference in absolute performance between the two training region conditions. However, generalization can be readily compared between the two conditions based on the performance of the test set of the non-trained-upon region relative to the performance of the test set from the training region.

Statistical analyses

A threshold of $\alpha=0.05$ was used for all statistical tests. An exception was the threshold used for tagging the units, namely for determining whether a unit exhibits light activation, and whether two units exhibit

406 monosynaptic connectivity ($\alpha=0.001$). All descriptive statistics (n, median, IQR) can be found in the
407 results, figures, tables, and legends. Differences between the medians of two unpaired groups were
408 compared using Mann-Whitney's *U*-test (two-tailed unless otherwise specified). Differences between
409 the median of a single group and a number, or between the medians of two paired groups, were
410 compared using Wilcoxon's signed-rank test (one-tailed unless otherwise specified). Comparisons of
411 more than two groups were conducted using Kruskal-Wallis one-way non-parametric analysis of
412 variance, and corrected for multiple comparisons using Tukey's procedure. Rank (Spearman's)
413 correlation coefficients were tested using a permutation test. All statistical tests were conducted using
414 either *SciPy* library (Virtanen et al., 2020) or custom code implemented in Python and MATLAB.

415

416 **Code accessibility**

417 The code used for feature extraction, model training, and visualization is freely available on GitHub
418 (<https://github.com/EranStarkLab/SpatiotemporalSpiking>).

Results

PYR and PV interneurons are tagged in freely-moving mice

Differentiating between PYR and PV cells based on electrical properties requires a ground truth labeled dataset. We recorded and tagged extracellular spiking data from freely-moving PV::ChR2 mice ($n=7$) using chronically-implanted four-shank, 32-channel optoelectronic arrays (**Fig. 1Aa**). Every shank was equipped with a diode-coupled fiber, enabling independent illumination of small local groups of neurons while concurrently recording the extracellular activity (**Fig. 1Ab**). We used 50-70 ms light pulses for optical tagging. A unit was tagged as PV if the stimulus-locked firing rate increase was consistently above baseline ($p<0.001$, Poisson test; **Fig. 1Ac**). Using the optical tagging procedure, a total of 27 units from the neocortex and 71 from CA1 were tagged as PV cells.

For every pair of simultaneously-recorded units, we calculated the spike-to-spike CCH and tested for peaks in the monosynaptic time range (0-5 ms; $p<0.001$, Bonferroni-corrected Poisson test). Units that participated as a reference in a CCH that exhibited a significant peak were tagged as excitatory (**Fig. 1B**). Using the monosynaptic CCH analysis, 424 units were tagged as excitatory and 21 as inhibitory; 13/21 units were both inhibitory and optically-activated. Together with the optically-tagged PV cells and after removing invalid samples (*Materials and Methods*), the dataset consists of 512 units, of which 411 units (80.3%) are PYR (**Fig. 1C**).

Waveform-based and spike-timing features allow near-perfect classification of PYR and PV cells

Waveform-based spike properties differ between PYR and PV cells and are widely used for cell type classification (Barthó et al., 2004; Cardin et al., 2009; Stark et al., 2013). However, many classifiers employ waveform-based features in conjunction with features based on spike-timing, and previously-used spike-based classifiers have not been cross-validated. For every unit, we calculated $n=8$ features

443 based on the waveform of the main channel (e.g., *TTP-duration*, **Fig. 2A**; **Table 1**), defined as the channel
 444 with the largest magnitude of the TTP. After deriving features for every unit, we trained and tested
 445 classification models. The area under the curve (AUC) for the models was 0.995 [0.978 1] (median [IQR];
 446 $p=3.1 \times 10^{-10}$, Wilcoxon test compared to chance level, 0.5). Despite the high AUC, model performance
 447 improved when spikes were partitioned into chunks of 25, 50 and 200 spikes ($p < 0.05$, Wilcoxon test).
 448 Partitioning into 50-spike chunks increased the original AUC by 0.11 [0 0.55] % to 0.999 [0.989 1],
 449 $p=0.001$, Wilcoxon test; **Fig. 2B**). A feature importance (SHAP) analysis carried out on the models trained
 450 with 50-spike chunks (**Table 1**) indicated that the *TTP-duration* feature provided the largest contribution
 451 to the prediction (median [IQR] over all 50 instantiations: 0.25 [0.23 0.26], $p=0.001$, permutation test).
 452 The fact that the AUC is near unity means that models based strictly on waveform features achieve near-
 453 perfect classification.

454 While spike-timing information has been used for cell type classification before, most implementations
 455 also considered waveform-based features (Csicsvari et al., 1998; Frank et al., 2001; Viskontas et al.,
 456 2007). To directly test whether spike-timing alone can yield accurate classification, we derived $n=8$
 457 spike-timing features from the spike trains of every unit (e.g., *Uniform-distance*, **Fig. 2C**; **Table 2**). We
 458 conducted the training and evaluation process for the spike-timing modality as for the waveform-based
 459 classification. Without chunking, the AUC was 0.975 [0.957 0.986] ($p=3.8 \times 10^{-10}$, Wilcoxon test). The
 460 performance of the spike-timing models did not exhibit consistent improvement upon chunking ($p > 0.05$
 461 for all chunk sizes, Wilcoxon test). Nevertheless, the highest improvement in the AUC was achieved
 462 using 1,600-spike chunks, increasing performance by 0.28 [-0.39 0.74] % to yield an AUC of 0.977 [0.965
 463 0.987] ($p=0.07$, Wilcoxon test; **Fig. 2D**). SHAP analysis using models trained with 1,600-spike chunks
 464 (**Table 2**) attributed the highest importance to the D_{KL} -Long feature (0.19 [0.17 0.2]), followed by the
 465 *Uniform-distance* feature (0.14 [0.12 0.16]; $p < 0.002$ for both, *U*-test). The results suggest that both high-

frequency and low-frequency features contribute to differentiation between PYR and PV cells, allowing near-perfect performance.

Transforming multi-channel spike waveforms to event-based delta-like functions removes all waveform-based information and allows extracting purely spatial features

Having established a cross-validated pipeline for cell type classification from spike data, we turned to focus on spatial features. To limit the information to spatiotemporal features per se, we first removed all single-channel waveform information from the waveforms recorded over the eight channels using an event-based delta transformation (*Materials and Methods*; **Fig. 3A**). The procedure was applied to three distinct events: the first median crossing (FMC), the maximal negativity (NEG), and the second median crossing (SMC). The transformation yielded nearly identical main channel waveforms for all units (**Fig. 3B**). To determine whether the delta transformation indeed removed all single-channel waveform information, we used the transformed spikes as input for waveform-based feature extraction, followed by model training and testing. The classification models yielded chance level results. Specifically, the AUC was 0.5 [0.5 0.5] ($p=0.99$, Wilcoxon test; **Fig. 3C**). When using a naïve decision threshold of 0.5, the same class was predicted for every sample (**Fig. 3C**, inset). Thus, the delta-transformed waveforms are devoid of waveform-based information.

From the transformed waveforms recorded on the eight channels, $n=18$ spatial features were derived for every unit (**Table 3**). The features were partitioned into three families: time-based (**Fig. 3D**), graph-based (**Fig. 3E**), and value-based (**Fig. 3F**; *Materials and Methods*). 10/18 (56%) of the spatial features exhibited differences between the PYR and PV populations ($p<0.05$, U -test). To estimate feature redundancy, we computed rank CCs and MI between every pair of spatial features. The matrix of CCs between spatial features (Extended Data **Fig. 3-1**) showed absolute correlations (median [IQR]: 0.2 [0.1 0.33]) that were smaller than for the waveform-based features (0.43 [0.2 0.77]; $p=3.5\times10^{-4}$, U -test) and

490 for the spike-timing features (0.52 [0.38 0.7]; $p=1.1\times 10^{-7}$). Furthermore, mutual information (MI) values
 491 between spatial feature distributions were smaller than MI between waveform-based features
 492 ($p<7.1\times 10^{-9}$, *U*-test) and smaller than MI between spike-timing features ($p<4.3\times 10^{-9}$). Moreover, absolute
 493 inter-modality CCs (0.13 [0.07 0.20]) were smaller than absolute intra-modality CCs (0.244 [0.13 0.48];
 494 $p=3.1\times 10^{-19}$, *U*-test). The weak correlations between spatial and waveform-based features, and between
 495 spatial and spike-timing features, suggest that a combination of features from different modalities may
 496 be beneficial for classification. Finally, the differences between the PYR and PV groups for most spatial
 497 features, together with the relatively weak mutual information between pairs of spatial features,
 498 suggest that the various spatial features may contain non-overlapping information useful for
 499 classification.

500

501 **The variance of spatial features over channels and across chunks is different for PYR and for PV cells**

502 A direct comparison of the spatiotemporal dispersion of the event times between PYR and PV cells
 503 revealed event-dependent synchronization differences for both cell types ($p<4.5\times 10^{-20}$, Kruskal-Wallis
 504 test; **Fig. 4A**). For PYR, an increase in spatiotemporal synchronization from FMC to NEG was observed
 505 (exhibited by a decrease in the SD; FMC: 15.9 [8.8 26.3] μ s; NEG: 13.5 [7.7 23.5] μ s; $p<0.02$, Kruskal-
 506 Wallis test, corrected for multiple comparisons). An increase from FMC to NEG was also seen for PV cells
 507 (FMC: 40.6 [17.4 86.3] μ s; NEG: 9.4 [5.4 13.3] μ s; $p<1\times 10^{-19}$). For both cell types, the increase in
 508 synchronization was followed by a decrease from NEG to SMC (SMC: PYR: 26 [18.8 34.3] μ s, $p<2.2\times 10^{-16}$;
 509 PV: 24.1 [15.6 38.9] μ s, $p<3.6\times 10^{-11}$). Thus, for both PYR and PV cells, spatiotemporal synchronization
 510 changes during the course of an action potential.

511 Next, we assessed whether PYR and PV cells exhibit differences in spatiotemporal synchronization
 512 during specific events. Higher spatiotemporal synchronization was observed for PYR spikes compared to
 513 PV cells during FMC, expressed by lower SD ($A_w=0.72$; $p=2.3\times 10^{-12}$, *U*-test; **Table 3**). Thus, the FMC event

occurred on multiple channels nearly at the same time for PYR spikes, whereas for PV cell spikes the FMC was more dispersed in time. Synchronization flipped during the NEG event, with higher synchronization for the PV cell spikes ($A_w=0.63$; $p=3.44\times10^{-5}$, U -test). We did not observe consistent differences during the SMC event ($A_w=0.50$; $p=0.47$, U -test). Similar changes between events were observed for the *Time-lag-SS* and the *Shortest-path* features (Extended Data **Fig. 4-1**). The synchronization differences between the spikes of PYR and PV cells may reflect the distinct morphological and functional properties of the different cell types.

Intra-unit variability, the variability across the chunks of the same unit, may degrade classification performance. Alternatively, intra-unit variability may differ between classes and possibly benefit classification. Of the statistics extracted from the chunks, the SD is a second moment statistic, and may hold unique information compared to the other chunk statistics employed. Specifically, we examined the intra-unit SD values for all spatial features calculated based on 25-spike chunks (the smallest chunk size employed). To allow comparing SDs of multiple features, features were scaled based on all units before calculating the SD for every unit. Most (13/18) features showed consistent differences of the SD between the PYR and PV cells groups ($0.56\leq A_w\leq 0.90$; $p<0.05$, U -test; **Table 4**). All features that did not differ consistently between the two cell types were of the graph-based family (*FMC-Average-weight*, *SMC-Average-weight*, *SMC-Longest-path*, *FMC-Shortest-path*, and *SMC-Shortest-path*; $0.50\leq A_w\leq 0.54$; $p>0.05$, U -test; **Fig. 4B**, gray lines). All the features that consistently differed between the two cell types exhibited larger SD values for PV cells, compared to PYR (**Fig. 4B**, black lines). The median SDs for all features were lower for PYR (0.34 [0.16 0.47]) compared to PV cells (0.53 [0.3 0.6]; $p=1.9\times10^{-4}$, Wilcoxon test). The higher intra-unit variability for PV cells indicates a common phenomenon of the spatial features that is identified specifically by chunking.

Features based exclusively on spatial information allow accurate classification of PYR and PV cells

To determine whether the differences between the spatial distribution of the extracellular signals from PYR and PV cells are only correlative or indicative, we conducted a training and evaluation process. The process was carried in the same manner as for the waveform-based and spike-timing features. Using the mean waveforms, the median [IQR] AUC was 0.83 [0.8 0.85] ($p=3.8\times 10^{-10}$, Wilcoxon test; **Fig. 5**). The performance of the spatial models improved when chunking was applied: chunking consistently increased the performance for all tested chunk sizes (25-1,600 spikes: $p<1.45\times 10^{-9}$, Wilcoxon test; **Fig. 5A**). Upon chunking to 1,600-spike chunks, the AUC increased by 9.6% compared to the no-chunking AUC. The AUC increased monotonically for progressively smaller chunk sizes, achieving a value of 0.963 [0.949 0.975] for 25-spike chunks (16.3 [13.9 19.6] % increase; **Fig. 5B**). We did not test smaller chunk sizes. Therefore, results reported from this point onwards are based on the best model, using 25-spike chunks. While the performance of the spatial models was lower than the performance of waveform-based or spike-timing models ($p<6.6\times 10^{-6}$ for both, two-tailed Wilcoxon test), the results indicate that PYR and PV cells can be accurately differentiated based on purely spatial features. On their own, spatial properties provide a completely new approach to cell type classification.

To assess the contribution of every spatial feature and family of features, we analyzed SHAP values. We found that feature importance was not uniform (**Fig. 5C**). Specifically, the highest importance was attributed to features derived from the FMC events (median [IQR] over all 50 instantiations: *FMC-Time-lag-SS*: 0.094 [0.087 0.1] and *FMC-Time-lag-SD*: 0.093 [0.086 0.099]; $p<0.001$ for both, permutation test; **Fig. 5C**). The feature families differed in the contribution to the prediction ($p<1.7\times 10^{-29}$, Kruskal-Wallis test). Features of the value-based family exhibited the lowest summed importance values (0.028 [0.021 0.036]), while the two other families reached higher values (time-based: 0.25 [0.23 0.27], graph-based: 0.11 [0.1 0.13], $p=2.6\times 10^{-8}$ for both, Kruskal-Wallis test corrected for multiple comparisons). The importance of the time-based features was the largest (time-based compared to graph-based: $p=2.6\times 10^{-8}$).

⁸). The distribution of the six most important features is shown in Extended Data Fig. 5-1. The feature importance analysis suggests that features agnostic to the physical distance between channels and features that do consider spatial locations make non-overlapping contributions to classification. Moreover, the usage of multiple features derived from the same event, the FMC, is beneficial.

Spatial models generalize poorer than waveform models but better than spike-timing models

In the tagged dataset, units were recorded from both CA1 and neocortex, allowing to test inter-region generalization. To quantify similarities between regions, we determined the performance of models trained using data from a single region on one test set from the training region, and on another test set from the non-trained-upon region. Training on either CA1 data or neocortical data, all models performed above chance level when tested on both the CA1 test set and the neocortical test set ($p < 7.5 \times 10^{-10}$ for all comparisons, Wilcoxon test; Fig. 6A, Extended Data Fig. 6-1). Specifically, spatial models trained on CA1 data reached median [IQR] AUC of 0.966 [0.934, 0.979] when tested on CA1 data and 0.83 [0.805 0.858] when tested on neocortical data. Complimentarily, when trained on neocortical data, spatial models reached an AUC of 0.923 [0.833 1] on the neocortical test set, and an AUC of 0.893 [0.86 0.918] on the CA1 test set. Comparing AUCs of the non-trained-upon region, performance was lower for the spike-timing models compared to the waveform-based models ($p < 2.2 \times 10^{-16}$ for both comparisons, Kruskal-Wallis test corrected for multiple comparisons; Fig. 6A). Likewise, performance was lower for the spike-timing models, compared to the spatial models ($p < 0.005$ for both comparisons; Fig. 6A). Thus, while all modalities generalize from CA1 to neocortex and from neocortex to CA1, waveform-based models allow the best performance whereas spike-timing models perform the worst.

Above-chance performance on the test set of the non-trained-upon region does not guarantee perfect generalization. To quantify generalization, we defined a “generalization error” as the relative decrease when comparing performance on the test set of the training region and performance on the test set of

the non-trained-upon region. The generalization error was consistently above zero for spatial models trained on data from either region, and for CA1-trained spike-timing models ($p < 0.05$ for all three comparisons, Wilcoxon test; **Fig. 6B**). For both training sets, waveform-based models showed lower errors than spatial models ($p < 0.05$ for both comparisons, Kruskal-Wallis test corrected for multiple comparisons; **Fig. 6C**). In addition, for the CA1-trained models, the generalization error of the spatial models was lower than that of the spike-timing models ($p < 6.7 \times 10^{-6}$). Thus, spatial models generalize better than spike-timing models, but worse than waveform-based models, in particular when trained on CA1 data.

Finally, to determine which spatial features are most important for classification in every region, we computed SHAP values for spatial models trained on data from a single region. Despite some differences in specific values, the six features that made the largest contributions were the same for models trained on CA1 data (Extended Data **Fig. 6-2A**) and for models trained on neocortical data (**Fig. 6-2B**; see also **Fig. 5C**). Hence, the determinants for the predictions of the spatial models are similar in neocortical and CA1 data.

Discussion

Using optically-tagged high-density recordings from hippocampal region CA1 and neocortex of freely-moving mice, we found that spiking of PYR and PV cells was associated with different spatiotemporal distributions of extracellular voltage. Compared to PV cell spikes, PYR spikes exhibited higher spatial synchrony at the beginning of the spike and lower synchrony at the trough. Together, the spatial features derived from the extracellular voltage distributions allowed accurate classification of PYR and PV cells.

Differences in the spatial distribution of extracellular voltages during spikes

Although the contribution of spatial information to classification tasks has been explored before (Buccino et al., 2018; Jia et al., 2019), previous work did not separate spatial information from other waveform-based properties. Utilizing an event-based delta transformation, we derived spatial features devoid of single-channel waveform information. The accurate classification based on spatial features is tantamount to spatiotemporal differences in the extracellular voltage distribution, and is consistent with morphological differences in the dendro-somatic and axonal organization of PYR and PV cells. In CA1, PV basket cell axons form a diverse horizontal network while most dendrites extend vertically (Freund and Buzsáki, 1996; Klausberger et al., 2003). The dendritic trees of PYR also extend vertically, but are more polarized (Bannister and Larkman, 1995; Spruston, 2008). The extracellular expression of intracellular signals has been studied theoretically (Rall, 1962) and modeled for reconstructed morphologies (Holt and Koch, 1999; Gold et al., 2006; Schomburg et al., 2012; Lindén et al., 2014; Bestel et al., 2021). Even with limited spatial sampling, the present results provide direct experimental evidence for a unique mapping between cell type and the spatial distribution of extracellular potentials. The results should be

622 construed as lower bounds, since higher density or three-dimensional sampling may allow further
623 improvement.

624 Among spatial features, the dispersion of the first median crossing (FMC) event between recording
625 sites made the highest contribution to the prediction. The FMC is a putative extracellular analogue of
626 the initial depolarization phase at the recording site. Thus, the lower inter-electrode variance of FMC
627 among PYR compared to PV cells indicates higher spatial synchrony at the beginning of the spike. This
628 observation is consistent with known morphological and electrotonic differences between the proximal
629 dendrites of PYR and PV cells. Since the probes were always inserted perpendicularly to CA1 str.
630 pyramidale, the vertical dendritic tree of both PYR and PV cells was parallel to the extracellular electrode
631 arrays. In CA1, PYR have thick apical dendrites extending for up to 250 μm (1.6-2.5 μm in diameter),
632 whereas PV cell dendrites in str. pyramidale are thinner (1.3-1.7 μm in diameter; Gulyás et al., 1999;
633 Andersen et al., 2007). The higher FMC synchrony of PYR spikes is consistent with lower axial resistance
634 of the thicker proximal PYR dendrites, yielding synchronized somatic and dendritic potentials.

635 The second event that showed differences in temporal dispersion was the maximal negativity (NEG),
636 which corresponds to a point between the peak of the derivative and the peak of membrane potential
637 during the spike (Henze et al., 2000; Pettersen and Einevoll, 2008). During NEG, spatial synchrony
638 reverses, being higher for PV compared to PYR. The narrower waveforms of PV cells are associated with
639 a higher concentration of voltage-gated K^+ (Kv) channels, compared to PYR (Bean, 2007). In neuronal
640 models with passive dendrites and when membrane time constants are relatively slow, membrane
641 resistance has little effect on spike shape (Pettersen and Einevoll, 2008). However, since active
642 conductance affects spike shape (Martina and Jonas, 1997), the differences in synchrony during the NEG
643 event may result from distinct spatial gradients of Kv channels in CA1 PYR and PV basket cells. In PYR,
644 there is rapid decrease in the density of Kv channels on dendrites farther from the soma (Johnston et al.,
645 2000), whereas the decrease for basket cells is more moderate (Hu et al., 2010). Kv channels open at

depolarization, initiating repolarization and late hyperpolarization and in turn, govern the frequency and the width of the spikes (Pongs, 1999). The more uniform spatial density of Kv channels in PV cells compared to PYR may synchronize the extracellular signals generated by the different cellular compartments.

The spatial features exhibit lower intra-unit variability of PYR, compared to PV cells. The difference between the PYR and PV variability contributed to classification. The excitatory input of PYR in CA1 originates mainly from upstream regions (e.g., CA3 and entorhinal cortex; Andersen et al., 2007), whereas CA1 PV cells are mainly innervated by local PYR (Freund and Buzsáki, 1996). Thus, a possible source for the difference in intra-unit variability is the distinct sources of excitation of PYR and PV cells.

Differences in spike waveform and spike-timing

Compared to basket cells, neocortical and CA1 PYR have wider spikes (Simons, 1978; Connors et al., 1982; Kawaguchi and Hama, 1988; Contreras 2004), lower firing rates (Kawaguchi et al., 1987), and an increased burst propensity (Kandel and Spencer, 1961; Ranck, 1973; Harris et al., 2001). Indeed, we found that waveform width (e.g., *TTP-duration*), burstiness (e.g., *Uniform-distance*), and firing rate, all differ between PYR and PV cells. Furthermore, both *TTP-duration* in the waveform models, and the *Uniform-distance* in the spike-timing models, contributed to the prediction. The importance of waveform width properties is in line with studies that used width-related features to differentiate between PYR and interneurons (Frank et al., 2001; Cardin et al., 2009; Stark et al., 2013). Similarly, the importance of burstiness and firing rate is consistent with prior work (Connors and Gutnick, 1990; Taira and Georgopoulos, 1993). The long-term ACH, which was not used before for classification, held informative value, consistent with distinct low frequency rhythmic activity of PYR and PV cells (e.g., theta; Csicsvari et al., 1999; Buzsáki, 2002; Czurkó et al., 2011).

Chunking

When discussing the extracellular waveform of a neuron, many studies refer to the mean waveform (e.g., Trainito et al., 2019; Sun et al., 2021). To improve the performance of the classification models, we exploited the variability of spike waveforms and timing recorded from a single cell using chunking, increasing the number of samples at the possible cost of increased noise. The chunking method as implemented here was agnostic to two pieces of information. First, spikes were randomly assigned to chunks, ignoring possible time-related changes that may be constructive. Second, the relation of chunks to the same unit was only partially considered, and additional “chunk statistics” may be extracted. The statistics extracted from the distribution of feature values over chunks provide limited consideration of the other chunks. Consequently, the present implementation does not allow classification of all the chunks of a specific unit as a whole. Hence, our results form a lower bound for the improvement to be gained from chunking. More complex models may capitalize on time-dependent differences and dependencies between the samples. Modifying chunk size inherently results in a tradeoff between the number of samples and the noise. Spatial and waveform-based models benefited the most from smaller chunks, while spike-timing models benefited from larger chunk sizes. The higher sensitivity of spike-timing models to noise in small chunks is consistent with the discrete nature of the spike trains, because ACHs are sparse when the number of spikes is small.

Inter-region differences

Waveform models yielded near-perfect classification of data from the non-trained-upon region for both training regions, in line with similar waveform widths of PYR and PV cells in neocortex and CA1 (McCormick et al., 1985; Kawaguchi and Hama, 1988). Yet, the generalization of waveform models was not perfect, and is not expected to be universal: in the primate, pyramidal tract PYR exhibit narrow spikes (Vigneswaran et al., 2011; Lemon et al., 2021). CA1-trained spike-timing and spatial models

694 exhibited decreased performance when tested on neocortical data compared to CA1 data, with spatial
695 models generalizing better than spike-timing models. The poor generalization observed for the spike-
696 timing models is consistent with the fact that neocortical PYR are less likely to exhibit bursts, compared
697 to CA1 PYR (McCormick et al., 1985; Lacaille et al., 1987). The intermediate generalization of the spatial
698 models may correspond to inter-region differences in cellular morphology, ion channel distributions, or
699 other cellular-network properties. The synaptic and intracellular events that occur just before and
700 during the spike may affect the spatial distribution of the signal (Zador et al., 1995; Hagen et al., 2016,
701 2017). Hence, even morphologically identical cells with the exact same compartmental distribution of
702 ion channels are expected to show different spatial distributions of extracellular potentials when
703 embedded in distinct networks.

704

705 **Limitations and applications**

706 There are a few notable limitations to this work. First, cell type classification based on spatial features
707 requires sampling the extracellular space over multiple points. Here, we employed a fixed electrode
708 configuration with 20 μm vertical spacing, and application to data recorded using other configurations
709 may require modifications. Second, expanding the duration of the sampled spikes beyond 1.6 ms (32
710 samples at 20 kHz) may increase the performance of spatial-based models. Third, while several models
711 yielded near-perfect performance, focusing strictly on mice does not warrant generalization to
712 homological brain regions in other animals.

713 Our results suggest several possible applications. First, the concept of chunking combined with a
714 majority vote can be used in real-time, allowing to update classification outcomes online. Using the
715 chunking and voting approach, there is no need to rerun the entire model whenever a new piece of data
716 is collected. Instead, every time a predetermined number of spikes is gathered, another vote can be

added to the prediction. Second, classification based strictly on spike-timing can be used when waveform information is unavailable, or for real-time applications.

Future directions

To identify the cellular-network origin of the spatiotemporal differences in synchrony between PYR and PV cells, targeted experiments may be conducted. We hypothesize that the higher intra-unit variability observed for PV cells compared to PYR may reflect distinct connectivity patterns. The excitatory input of PYR in CA1 originates mainly from upstream regions (e.g., CA3 and entorhinal cortex; Andersen et al., 2007), whereas CA1 PV cells are more likely to be innervated by local PYR (Freund and Buzsáki, 1996). The hypothesis may be tested using somatic opsins (e.g., Shemesh et al., 2017; Chen et al., 2018; Forli et al., 2021). The spatiotemporal distribution of extracellular potentials during spikes generated via somatic activation can be compared to natural spiking, generated by integrating excitatory postsynaptic potentials impinging mainly on the dendrites. More consistent spatiotemporal synchrony achieved for optically-induced spikes will provide direct evidence that input variability may lead to more variability in the spatiotemporal synchrony.

In the future, other spatial features may be used to increase classification performance. We showed that the cross-validated classification of PYR and PV cells is already near-perfect when based on waveforms alone, but other cell types may not be accurately distinguished using features derived from a single channel. For instance, compared to PV cells, somatostatin interneurons have lower firing rates and broader spikes (Ma et al., 2010; Royer et al., 2012; Veit et al., 2017). Distinguishing between multiple cell types using extracellular data may benefit from using spatial information.

References

- Andersen P, Morris R, Amaral D, Bliss T, O'Keefe J (2007) The hippocampus book. New York, NY: Oxford University Press.
- Archer KJ, Kimes RV (2008) Empirical characterization of random forest variable importance measures. *Comput Stat Data Anal* 52:2249-2260.
- Ascoli GA, Donohue DE, Halavi M (2007) NeuroMorpho. Org: a central resource for neuronal morphologies. *J Neurosci* 27:9247-9251.
- Bannister NJ, Larkman AU (1995) Dendritic morphology of CA1 pyramidal neurones from the rat hippocampus: I. Branching patterns. *J Comp Neurol* 360:150-160.
- Barthó P, Hirase H, Monconduit L, Zugaro M, Harris KD, Buzsáki G (2004). Characterization of neocortical principal cells and interneurons by network interactions and extracellular features. *J Neurophysiol* 92:600-608.
- Bean BP (2007) The action potential in mammalian central neurons. *Nat Rev Neurosci* 8:451-465.
- Bestel, R, van Rienen U, Thielemann C, Appali R (2021) Influence of neuronal morphology on the shape of extracellular recordings with microelectrode arrays: A finite element analysis. *IEEE Trans Biomed Eng* 68:1317-1329.
- Breiman L (1996) Bagging predictors. *Mach Learn* 24:123-140.
- Breiman L (2001) Random forests. *Mach Learn* 45:5-32.

- 756 Brodmann K (1909) Vergleichende Lokalisationslehre der Grosshirnrinde in ihren Prinzipien dargestellt
757 auf Grund des Zellenbaues. Barth.
- 758 Buccino AP, Kordovan M, Ness TV, Merkt B, Häfliger PD, Fyhn M, Cauwenberghs G, Rotter S, Einevoll
759 GT (2018) Combining biophysical modeling and deep learning for multielectrode array neuron
760 localization and classification. *J Neurophysiol* 120:1212-1232.
- 761 Buzsáki G (2002) Theta oscillations in the hippocampus. *Neuron* 33:325-340.
- 762 Buzsáki G (2004) Large-scale recording of neuronal ensembles. *Nat Neurosci* 7:446-451.
- 763 Cardin JA, Carlén M, Meletis K, Knoblich U, Zhang F, Deisseroth K, Tsai LH, Moore CI (2009) Driving fast-
764 spiking cells induces gamma rhythm and controls sensory responses. *Nature* 459:663-667.
- 765 Chen IW, Papagiakoumou E, Emiliani V (2018) Towards circuit optogenetics. *Curr Opin Neurobiol*
766 50:179-189.
- 767 Clasca F, Rubio-Garrido P, Jabaudon D (2012) Unveiling the diversity of thalamocortical neuron
768 subtypes. *Eur J Neurosci* 35:1524-1532.
- 769 Connors BW, Gutnick MJ (1990) Intrinsic firing patterns of diverse neocortical neurons. *Trends*
770 *Neurosci* 13:99-104.
- 771 Connors BW, Gutnick MJ, Prince DA (1982) Electrophysiological properties of neocortical neurons in
772 vitro. *J Neurophysiol* 48:1302-1320.
- 773 Contreras D (2004) Electrophysiological classes of neocortical neurons. *Neural Netw* 17:633-646.

- 774 Csicsvari J, Hirase H, Czurko A, Buzsáki G (1998) Reliability and state dependence of pyramidal cell-
 775 interneuron synapses in the hippocampus: an ensemble approach in the behaving rat. *Neuron* 21:179-
 776 189.
- 777 Csicsvari J, Hirase H, Czurkó A, Mamiya A, Buzsáki G (1999) Oscillatory coupling of hippocampal
 778 pyramidal cells and interneurons in the behaving rat. *J Neurosci* 19:274-287.
- 779 Czurkó A, Huxter J, Li Y, Hangya B, Muller RU (2011) Theta phase classification of interneurons in the
 780 hippocampal formation of freely moving rats. *J Neurosci* 31:2938-2947.
- 781 Einevoll GT, Kayser C, Logothetis NK, Panzeri S (2013) Modelling and analysis of local field potentials
 782 for studying the function of cortical circuits. *Nat Rev Neurosci* 14:770-785.
- 783 Esposito C, Landrum GA, Schneider N, Stiefl N, Riniker S (2021) GHOST: adjusting the decision
 784 threshold to handle imbalanced data in machine learning. *J Chem Inf Model* 61:2623-2640.
- 785 Fawcett T (2006) An introduction to ROC analysis. *Pattern Recognit Lett* 27:861-874.
- 786 Fee MS, Mitra PP, Kleinfeld D (1996) Automatic sorting of multiple unit neuronal signals in the
 787 presence of anisotropic and non-Gaussian variability. *J Neurosci Methods* 69:175-188.
- 788 Forli A, Pisoni M, Printz Y, Yizhar O, Fellin T (2021) Optogenetic strategies for high-efficiency all-optical
 789 interrogation using blue-light-sensitive opsins. *Elife* 10:e63359.
- 790 Frank LM, Brown EN, Wilson MA (2001) A comparison of the firing properties of putative excitatory
 791 and inhibitory neurons from CA1 and the entorhinal cortex. *J Neurophysiol* 86:2029-2040.
- 792 Freund TF, Buzsáki G (1996) Interneurons of the hippocampus. *Hippocampus* 6:347-470.

- 793 Fujishima K, Kawabata Galbraith K, Kengaku M (2018) Dendritic self-avoidance and morphological
794 development of cerebellar purkinje cells. *Cerebellum* 17:701-708.
- 795 Ganter P, Szücs P, Paulsen O, Somogyi P (2004) Properties of horizontal axo-axonic cells in stratum
796 oriens of the hippocampal CA1 area of rats in vitro. *Hippocampus* 14:232-243.
- 797 Gold C, Henze DA, Koch C, Buzsáki G (2006) On the origin of the extracellular action potential
798 waveform: a modeling study. *J Neurophysiol* 95:3113-3128.
- 799 Gold C, Girardin CC, Martin KA, Koch C (2009) High-amplitude positive spikes recorded extracellularly
800 in cat visual cortex. *J Neurophysiol* 102:3340-3351.
- 801 Gulyás AI, Megias M, Emri Z, Freund TF (1999) Total number and ratio of excitatory and inhibitory
802 synapses converging onto single interneurons of different types in the CA1 area of the rat hippocampus.
803 *J Neurosci* 19:10082-10097.
- 804 Hagen E, Dahmen D, Stavrinou ML, Lindén H, Tetzlaff T, Van Albada SJ, Grün S, Diesmann M, Einevoll
805 GT (2016) Hybrid scheme for modeling local field potentials from point-neuron networks. *Cereb Cortex*
806 26:4461-4496.
- 807 Hagen E, Fossum JC, Pettersen KH, Alonso JM, Swadlow HA, Einevoll GT (2017) Focal local field
808 potential signature of the single-axon monosynaptic thalamocortical connection. *J Neurosci* 37:5123-
809 5143.
- 810 Harris KD, Henze DA, Csicsvari J, Hirase H, Buzsáki G (2000) Accuracy of tetrode spike separation as
811 determined by simultaneous intracellular and extracellular measurements. *J Neurophysiol* 84:401-414.
- 812 Harris KD, Hirase H, Leinekugel X, Henze DA, Buzsáki G (2001) Temporal interaction between single
813 spikes and complex spike bursts in hippocampal pyramidal cells. *Neuron* 32:141-149.

- 814 Henze DA, Borhegyi Z, Csicsvari J, Mamiya A, Harris KD, Buzsaki G (2000) Intracellular features
815 predicted by extracellular recordings in the hippocampus in vivo. *J Neurophysiol* 84:390-400.
- 816 Henze DA, Wittner L, Buzsáki G (2002) Single granule cells reliably discharge targets in the hippocampal
817 CA3 network in vivo. *Nat Neurosci* 5:790-795.
- 818 Holt GR, Koch C (1999) Electrical interactions via the extracellular potential near cell bodies. *J Comput*
819 *Neurosci* 6:169-184.
- 820 Hong G, Lieber CM (2019) Novel electrode technologies for neural recordings. *Nat Rev Neurosci*
821 20:330-345.
- 822 Hu H, Martina M, Jonas P (2010) Dendritic mechanisms underlying rapid synaptic activation of fast-
823 spiking hippocampal interneurons. *Science* 327:52-58.
- 824 Jia X, Siegle JH, Bennett C, Gale SD, Denman DJ, Koch C, Olsen SR (2019) High-density extracellular
825 probes reveal dendritic backpropagation and facilitate neuron classification. *J Neurophysiol* 121:1831-
826 1847.
- 827 Johnston D, Hoffman DA, Magee JC, Poolos NP, Watanabe S, Colbert CM, Migliore M (2000) Dendritic
828 potassium channels in hippocampal pyramidal neurons. *J Physiol* 525:75-81.
- 829 Jones EG (2012) *The Thalamus*. New York, NY: Springer Science & Business Media.
- 830 Jun JJ, Steinmetz NA, Siegle JH, Denman DJ, Bauza M, Barbarits B, Lee AK, Anastassiou CA, Andrei A,
831 Aydın Ç, Barbic M, Blanche TJ, Bonin V, Couto J, Dutta B, Gratiy SL, Gutnisky DA, Häusser M, Karsh B,
832 Ledochowitsch P, Lopez CM, Mitelut C, Musa S, Okun M, Pachitariu M, Putzeys J, Rich PD, Rossant C, Sun
833 WL, Svoboda K, Carandini M, Harris KD, Koch C, O'Keefe J, Harris TD (2017) Fully integrated silicon
834 probes for high-density recording of neural activity. *Nature* 551:232-236.

- 835 Kandel ER, Spencer WA (1961) Electrophysiology of hippocampal neurons: II. After-potentials and
 836 repetitive firing. *J Neurophysiol* 24:243-259.
- 837 Kawaguchi Y, Katsumaru H, Kosaka T, Heizmann CW, Hama K (1987) Fast spiking cells in rat
 838 hippocampus (CA1 region) contain the calcium-binding protein parvalbumin. *Brain Res* 416:369-374.
- 839 Kawaguchi Y, Hama K (1988) Physiological heterogeneity of nonpyramidal cells in rat hippocampal CA1
 840 region. *Exp Brain Res* 72:494-502.
- 841 Kepecs A, Fishell G (2014) Interneuron cell types are fit to function. *Nature* 505:318-326.
- 842 Klausberger T, Magill PJ, Márton LF, Roberts JDB, Cobden PM, Buzsáki G, Somogyi P (2003) Brain-state-
 843 and cell-type-specific firing of hippocampal interneurons in vivo. *Nature* 421:844-848.
- 844 Klausberger T, Somogyi P (2008) Neuronal diversity and temporal dynamics: the unity of hippocampal
 845 circuit operations. *Science* 321:53-57.
- 846 Kobayashi R, Kurita S, Kurth A, Kitano K, Mizuseki K, Diesmann M, Richmond BJ, Shinomoto S (2019)
 847 Reconstructing neuronal circuitry from parallel spike trains. *Nat Commun* 10:1-13.
- 848 Krstajic D, Buturovic LJ, Leahy DE, Thomas S (2014) Cross-validation pitfalls when selecting and
 849 assessing regression and classification models. *J Cheminform* 6:1-15.
- 850 Lacaille JC, Mueller AL, Kunkel DD, Schwartzkroin PA (1987). Local circuit interactions between
 851 oriens/alveus interneurons and CA1 pyramidal cells in hippocampal slices: electrophysiology and
 852 morphology. *J Neurosci* 7:1979-1993.
- 853 Lemon RN, Baker SN, Kraskov A (2021) Classification of cortical neurons by spike shape and the
 854 identification of pyramidal neurons. *Cereb Cortex* 31:5131-5138.

- 855 Li JCH (2016) Effect size measures in a two-independent-samples case with nonnormal and
 856 nonhomogeneous data. *Behav Res Methods* 48:1560-1574.
- 857 Lindén H, Hagen E, Leski S, Norheim ES, Pettersen KH, Einevoll GT (2014) LFPy: a tool for biophysical
 858 simulation of extracellular potentials generated by detailed model neurons. *Front Neuroinform* 7:41.
- 859 Lundberg SM, Erion G, Chen H, DeGrave A, Prutkin JM, Nair B, Katz R, Himmelfarb J, Bansal N, Lee SI
 860 (2020) From local explanations to global understanding with explainable AI for trees. *Nat Mach Intell*
 861 2:56-67.
- 862 Ma WP, Liu BH, Li YT, Huang ZJ, Zhang LI, Tao HW (2010) Visual representations by cortical
 863 somatostatin inhibitory neurons-selective but with weak and delayed responses. *J Neurosci* 30:14371-
 864 14379.
- 865 Maccaferri G, David J, Roberts B, Szucs P, Cottingham CA, Somogyi P (2000) Cell surface domain
 866 specific postsynaptic currents evoked by identified GABAergic neurones in rat hippocampus in vitro. *J*
 867 *Physiol* 524:91-116.
- 868 Magee JC, Johnston D (1995) Characterization of single voltage-gated Na⁺ and Ca²⁺ channels in apical
 869 dendrites of rat CA1 pyramidal neurons. *J Physiol* 487:67-90.
- 870 Markram H, Toledo-Rodriguez M, Wang Y, Gupta A, Silberberg G, Wu C (2004) Interneurons of the
 871 neocortical inhibitory system. *Nat Rev Neurosci* 5:793-807.
- 872 Martina M, Jonas P (1997) Functional differences in Na⁺ channel gating between fast-spiking
 873 interneurones and principal neurones of rat hippocampus. *J Physiol*, 505:593-603.
- 874 McCormick DA, Connors BW, Lighthall JW, Prince DA (1985) Comparative electrophysiology of
 875 pyramidal and sparsely spiny stellate neurons of the neocortex. *J Neurophysiol* 54:782-806.

- 876 McKay BE, Turner RW (2005) Physiological and morphological development of the rat cerebellar
877 Purkinje cell. *J Physiol* 567:829-850.
- 878 Mendoza G, Peyrache A, Gámez J, Prado L, Buzsáki G, Merchant H (2016) Recording extracellular
879 neural activity in the behaving monkey using a semichronic and high-density electrode system. *J*
880 *Neurophysiol* 116:563-574.
- 881 Mikołajczyk A, Grochowski M (2018) Data augmentation for improving deep learning in image
882 classification problem. In 2018 international interdisciplinary PhD workshop (IIPhDW) (pp. 117-122).
883 IEEE.
- 884 Monyer H, Markram H (2004) Interneuron Diversity series: Molecular and genetic tools to study
885 GABAergic interneuron diversity and function. *Trends Neurosci* 27:90-97.
- 886 Moreno-Barea FJ, Strazzera F, Jerez JM, Urda D, Franco L (2018) Forward noise adjustment scheme for
887 data augmentation. In 2018 IEEE symposium series on computational intelligence (SSCI) (pp. 728-734).
888 IEEE.
- 889 Pettersen KH, Einevoll GT (2008) Amplitude variability and extracellular low-pass filtering of neuronal
890 spikes. *Biophys J* 94:784-802.
- 891 Pawelzik H, Hughes DI, Thomson AM (2002) Physiological and morphological diversity of
892 immunocytochemically defined parvalbumin-and cholecystokinin-positive interneurons in CA1 of the
893 adult rat hippocampus. *J Comp Neurol* 443:346-367.
- 894 Pedregosa F, Varoquaux G, Gramfort A, Michel V, Thirion B, Grisel O, Blondel M, Prettenhofer P, Weiss
895 R, Dubourg V, Vanderplas J (2011) Scikit-learn: Machine learning in Python. *J Mach Learn Res* 12:2825-
896 2830.

- 897 Pongs O (1999) Voltage-gated potassium channels: from hyperexcitability to excitement. *FEBS Lett*
 898 452:31-35.
- 899 Rall W (1962) Electrophysiology of a dendritic neuron model. *Biophys J* 2:145–167.
- 900 Ramón y Cajal S (1909) *Histologie du systeme nerveux de l’homme et des vertebres*. Paris: Maloine.
- 901 Ranck JB Jr (1973) Studies on single neurons in dorsal hippocampal formation and septum in
 902 unrestrained rats: Part I. Behavioral correlates and firing repertoires. *Exp Neurol* 41:462-531.
- 903 Royer S, Zemelman BV, Losonczy A, Kim J, Chance F, Magee JC, Buzsáki G (2012) Control of timing, rate
 904 and bursts of hippocampal place cells by dendritic and somatic inhibition. *Nat Neurosci* 15:769-775.
- 905 Ruscio J (2008) A probability-based measure of effect size: robustness to base rates and other factors.
 906 *Psychol Methods*, 13:19-30.
- 907 Schmitzer-Torbert N, Jackson J, Henze D, Harris K, Redish AD (2005) Quantitative measures of cluster
 908 quality for use in extracellular recordings. *Neurosci* 131:1–11.
- 909 Schomburg EW, Anastassiou CA, Buzsáki G, Koch C (2012) The spiking component of oscillatory
 910 extracellular potentials in the rat hippocampus. *J Neurosci* 32:11798-11811.
- 911 Simons DJ (1978) Response properties of vibrissa units in rat SI somatosensory neocortex. *J*
 912 *Neurophysiol* 41:798-820.
- 913 Shemesh OA, Tanese D, Zampini V, Linghu C, Piatkevich K, Ronzitti E, Papagiakoumou E, Boyden ES,
 914 Emiliani V (2017) Temporally precise single-cell-resolution optogenetics. *Nat Neurosci* 20:1796-1806.
- 915 Sheng VS, Ling CX (2006) Thresholding for making classifiers cost-sensitive. *AAAI* 6:476-481.

- 916 Shobe JL, Claar LD, Parhami S, Bakhurin KI, Masmanidis SC (2015) Brain activity mapping at multiple
 917 scales with silicon microprobes containing 1,024 electrodes. *J Neurophysiol* 114:2043-2052.
- 918 Somogyi P, Klausberger T (2005) Defined types of cortical interneurone structure space and spike
 919 timing in the hippocampus. *J Physiol* 562:9-26.
- 920 Spruston N (2008) Pyramidal neurons: dendritic structure and synaptic integration. *Nat Rev Neurosci*
 921 9:206-221.
- 922 Stark E, Koos T, Buzsáki G (2012) Diode probes for spatiotemporal optical control of multiple neurons
 923 in freely moving animals. *J Neurophysiol* 108:349-363.
- 924 Stark E, Eichler R, Roux L, Fujisawa S, Rotstein HG, Buzsáki G (2013) Inhibition-induced theta resonance
 925 in cortical circuits. *Neuron* 80:1263-1276.
- 926 Steinmetz NA et al. (2021). Neuropixels 2.0: A miniaturized high-density probe for stable, long-term
 927 brain recordings. *Science* 372:eabf4588.
- 928 Sun SH, Almasi A, Yunzab M, Zehra S, Hicks DG, Kameneva T, Ibbotson MR, Meffin H (2021) Analysis of
 929 extracellular spike waveforms and associated receptive fields of neurons in cat primary visual cortex. *J*
 930 *Physiol* 599:2211-2238.
- 931 Taira M, Georgopoulos AP (1993) Cortical cell types from spike trains. *Neurosci Res* 17:39-45.
- 932 Tasic B et al. (2018) Shared and distinct transcriptomic cell types across neocortical areas. *Nature*
 933 563:72-78.
- 934 Timme NM, Lapish C (2018) A Tutorial for Information Theory in Neuroscience. *eNeuro*
 935 5:ENEURO.0052-18.2018.

- 936 Trainito C, von Nicolai C, Miller EK, Siegel M (2019) Extracellular spike waveform dissociates four
 937 functionally distinct cell classes in primate cortex. *Curr Biol* 29:2973-2982.
- 938 Tremblay R, Lee S, Rudy B (2016) GABAergic interneurons in the neocortex: from cellular properties to
 939 circuits. *Neuron* 91:260-292.
- 940 Troullinou E, Tsagkatakis G, Chavlis S, Turi GF, Li W, Losonczy A, Tsakalides P, Poirazi P (2020) Artificial
 941 neural networks in action for an automated cell-type classification of biological neural networks. *IEEE*
 942 *Trans Emerg Top Comput Intell* 5:755-767.
- 943 Varma S, Simon R (2006) Bias in error estimation when using cross-validation for model selection. *BMC*
 944 *Bioinform* 7:1-8.
- 945 Veit J, Hakim R, Jadi MP, Sejnowski TJ, Adesnik H (2017) Cortical gamma band synchronization through
 946 somatostatin interneurons. *Nat Neurosci* 20:951-959.
- 947 Vigneswaran G, Kraskov A, Lemon RN (2011) Large identified pyramidal cells in macaque motor and
 948 premotor cortex exhibit “thin spikes”: implications for cell type classification. *J Neurosci* 31:14235-
 949 14242.
- 950 Virtanen P et al. (2020) SciPy 1.0: fundamental algorithms for scientific computing in Python. *Nat*
 951 *Methods* 17:261-272.
- 952 Viskontas IV, Ekstrom AD, Wilson CL, Fried I (2007) Characterizing interneuron and pyramidal cells in
 953 the human medial temporal lobe in vivo using extracellular recordings. *Hippocampus* 17:49-57.
- 954 Yu J, Hu H, Agmon A, Svoboda K (2019) Principles governing the dynamics of GABAergic interneurons in
 955 the barrel cortex. *BioRxiv* 554949. <https://doi.org/10.1101/554949>

- 956 Zador AM, Agmon-Snir H, Segev I (1995) The morphoelectrotonic transform: a graphical approach to
957 dendritic function. *J Neurosci* 15:1669-1682.
- 958 Zeisel A, Muñoz-Manchado AB, Codeluppi S, Lönnerberg P, La Manno G, Juréus A, Marques S,
959 Munguba H, He L, Betsholtz C, Rolny C, Castelo-Branco G, Hjerling-Leffler J, Linnarsson S (2015) Cell
960 types in the mouse cortex and hippocampus revealed by single-cell RNA-seq. *Science* 347:1138-1142.
- 961 Zeng H, Sanes JR (2017) Neuronal cell-type classification: challenges, opportunities and the path
962 forward. *Nat Rev Neurosci* 18:530-546.

963 **Tables**

964

Feature	Family	Description	PYR median [IQR]	PV median [IQR]	Effect Size (A_w^{-1})	Cell type p -value ²	SHAP (p -value) ³
TTP ⁴ - duration	Waveform	The duration between the trough (maximal negativity) and the peak (maximal positivity) [ms]	0.77 [0.76 0.77]	0.29 [0.25 0.35]	0.98	5.9×10^{-58}	0.25 (0.001)
TTP- magnitude		The difference between the trough and the peak [AU] ⁵	1.4 [1.4 1.5]	1.3 [1.2 1.3]	0.97	3.7×10^{-48}	0.11 (0.003)
FWHM ⁶		The duration in which the value is at least -0.5 (i.e., half of the trough) [ms]	0.21 [0.2 0.23]	0.16 [0.15 0.18]	0.89	3.7×10^{-34}	0.005 (0.59)
Rise- coefficient		A straight line connects the trough and the last sample. The coefficient is the time from the trough to the point where the absolute distance from the line is maximal [ms]	0.29 [0.26 0.32]	0.24 [0.21 0.26]	0.80	2.2×10^{-21}	0.005 (0.99)

Max-speed	First time derivative ⁷	The duration after the trough, for which the spike maintains the same change rate (derivative) [ms]	0.19 [0.14 0.26]	0.14 [0.13 0.17]	0.69	3.4×10^{-9}	0.011 (0.41)
Break-measure	Second time derivative ⁷	The sum of the values of the second derivative just before the trough (0.3 to 0.08 ms before the trough) [10^{-1} *AU]	-0.67 [-0.76 -0.56]	-0.58 [-0.7 -0.49]	0.64	7.9×10^{-6}	0.003 (0.84)
Smile-cry		The sum of the values of the second derivative at the end of the spike (0.26 to 0.76 ms from the trough) [10^{-2} *AU]	-1.2 [-1.4 -1.1]	-0.3 [-0.9 -0.1]	0.89	5.7×10^{-35}	0.013 (0.044)
Acceleration		The sum of the squared values of the second derivative just after the trough (0.08 to 0.25 ms after the trough) [10^{-6} *AU ²]	9 [5 14]	91 [49 139]	0.97	6.8×10^{-49}	0.12 (0.002)

Table 1. Waveform-based features

⁷A_w ranges from 0.5 (no difference) to 1 (non-overlapping distributions).

968 ² Mann-Whitney *U*-test.

969 ³ Median Shapley additive explanations (SHAP) values based on 50-spike chunks, indicating feature
970 importance. Parentheses, *p*-values based on a one-tailed shuffle test.

971 ⁴ Trough-to-peak.

972 ⁵ The waveforms are scaled to the [-1 1] range. Thus, while the original units are μV , here we use
973 arbitrary units (AU).

974 ⁶ Full-width at half-maximum

975 ⁷ Derivatives were computed numerically as the difference between every two adjacent samples.

Feature	Family	Description	PYR median [IQR]	PV median [IQR]	Effect Size (A_w^{-1})	Cell type p -value ²	SHAP (p -value) ³
Uniform-distance	High frequency (0-50 ms) ⁴	The mean distance between the CDF of the ACH and the CDF of a uniform distribution	0.12 [0.09 0.16]	0.03 [0.02 0.04]	0.95	1.6×10^{-44}	0.14 (0.002)
D _{KL} -Short		The D _{KL} between the PDF of the ACH and the PDF of a uniform distribution	0.25 [0.17 0.34]	0.058 [0.037 0.079]	0.95	2.2×10^{-44}	0.025 (0.36)
Rise-time		The duration in which the values in the CDF of the ACH are above a threshold of 1/e [ms]	11.1 [9.4 13.7]	19.3 [17.8 20.6]	0.88	4.3×10^{-33}	0.031 (0.25)
Jump-index	Low frequency (50-1,000 ms) ⁴	The mean distance between the CDF of the ACH and the CDF of a uniform distribution	0.067 [0.044 0.088]	0.016 [0.0095 0.024]	0.92	9.3×10^{-39}	0.029 (0.31)
D _{KL} -Long		The D _{KL} between the PDF of the ACH and the PDF of a uniform distribution	0.069 [0.032 0.15]	0.0039 [0.0017 0.012]	0.89	6.1×10^{-35}	0.19 (0.001)
PSD-center	Wide-band (0-1,000)	The centroid of the power spectral density (PSD),	37 [33 42]	31 [26 37]	0.65	2.8×10^{-6}	0.016 (0.56)

	ms)	namely the squared FFT of the ACH [Hz]					
PSD'-center		The centroid of the derivative ⁵ of the PSD with respect to frequency [Hz]	23 [19 29]	21 [18 27]	0.57	0.012	0.009 (0.83)
Firing-rate		The average firing rate [spk/s]	0.69 [0.35 1.47]	8.95 [3.39 16.35]	0.93	1x10 ⁻⁴⁰	0.077 (0.038)

Table 2. Spike-timing features

¹ A_w ranges from 0.5 (no difference) to 1 (non-overlapping distributions).

² Mann-Whitney U -test.

³ Median Shapley additive explanations (SHAP) values based on 1,600-spike chunks, indicating feature importance. Parentheses, p -values based on a one-tailed shuffle test.

⁴ Most high-frequency and low-frequency features are based on distributions and therefore hold no units.

⁵ Derivatives were computed numerically as the difference between every two adjacent samples.

985

Feature	Family	Description	Event	PYR median [IQR]	PV median [IQR]	Effect Size (A_w^{-1})	Cell type p -value ²	SHAP (p -value) ³
Time-lag- SS ⁴	Time- based ⁵	The mean SS of the time offsets of the event [10 ³ *μs ²]	FMC	0.44 [0.13 1.39]	3.33 [0.49 12.02]	0.74	6.47x10 ⁻¹⁴	0.094 (0.001)
			NEG	0.34 [0.1 1.1]	0.16 [0.05 0.35]	0.64	7.04x10 ⁻⁶	0.008 (0.32)
			SMC	1.9 [0.77 3.45]	1.69 [0.68 3.48]	0.51	0.34	0.046 (0.015)
Time-lag- SD		The SD of the time offsets of the event [μs]	FMC	15.9 [8.8 26.3]	40.6 [17.4 86.3]	0.72	2.3x10 ⁻¹²	0.093 (0.001)
			NEG	13.5 [7.7 23.5]	9.4 [5.4 13.3]	0.63	3.44x10 ⁻⁵	0.009 (0.30)
			SMC	26 [18.8 34.3]	24.1 [15.6 38.9]	0.50	0.47	0.052 (0.006)
Average- weight	Graph- based	The average edge weight in the graph [mm/s]	FMC	2455 [1366 3509]	1206 [684 2577]	0.68	1.65x10 ⁻⁸	0.038 (0.027)
			NEG	2724 [1678 4269]	3633 [2173 5387]	0.61	3.13x10 ⁻⁴	0.007 (0.31)
			SMC	1844	2034	0.51	0.34	0.008

				[1232 2674]	[1099 2947]			(0.31)
Longest- path		The sum of weights in the longest path in the graph [mm/s]	FMC	6722 [3581 11514]	4909 [2417 9945]	0.58	0.0053	0.014 (0.18)
			NEG	8103 [4200 14436]	11517 [4923 16349]	0.55	0.06	0.006 (0.33)
			SMC	6050 [3269 11115]	6888 [3237 11056]	0.51	0.33	0.013 (0.21)
Shortest- path		The sum of weights in the shortest path in the graph [mm/s]	FMC	1049 [657 1619]	494 [267 928]	0.74	1.04x10 ⁻¹³	0.068 (0.001)
			NEG	1071 [714 1754]	1607 [916 2572]	0.63	1.4x10 ⁻⁵	0.006 (0.33)
	SMC		584 [426 872]	701 [409 1024]	0.55	0.08	0.008 (0.30)	
SPD- Count	Value- based ⁶	The number of values that crossed 0.5	-	2 [1 3]	2 [1 3]	0.55	0.06	0.007 (0.17)
SPD-SD		The SD of the vector	-	0.30 [0.28 0.33]	0.29 [0.27 0.31]	0.65	3.02x10 ⁻⁶	0.008 (0.32)
SPD-Area		The AUC ⁷	-	1.95 [1.45 2.54]	2.02 [1.64 2.44]	0.52	0.29	0.016 (0.19)

Table 3. Spatial features

988 ¹ A_w ranges from 0.5 (no difference) to 1 (non-overlapping distributions).

989 ² Mann-Whitney U -test.

990 ³ Median Shapley additive explanations (SHAP) values based on 25-spike chunks, indicating feature
991 importance. Parentheses, p -values based on a one-tailed shuffle test.

992 ⁴ Sum of squares

993 ⁵ Time offsets are relative to the main channel.

994 ⁶ Based on the vector of maximal negativity values for each channel, scaled to the [0 1] range. The
995 features are based on counts and thus hold no units.

996 ⁷ The area under the curve of the count of channels vs. the threshold value.

Feature	Event	PYR SD (scaled) ^{1,2}	PV SD (scaled) ^{1,2}	A _w ³	P-value ⁴
Time-lag-SS	FMC	0.065 [0.019 0.22]	0.67 [0.42 0.93]	0.90	8.9x10 ⁻³⁷
	NEG	0.033 [0.011 0.076]	0.037 [0.011 0.21]	0.56	0.022
	SMC	0.15 [0.097 0.23]	0.51 [0.25 0.83]	0.83	1.1x10 ⁻²⁵
Time-lag-SD	FMC	0.19 [0.093 0.41]	0.80 [0.61 0.94]	0.90	1.3x10 ⁻³⁵
	NEG	0.19 [0.10 0.32]	0.23 [0.12 0.48]	0.56	0.02
	SMC	0.32 [0.26 0.42]	0.70 [0.50 0.93]	0.85	1.6x10 ⁻²⁷
Average-weight	FMC	0.61 [0.36 0.84]	0.61 [0.41 0.76]	0.50	0.46
	NEG	0.43 [0.28 0.62]	0.48 [0.36 0.68]	0.57	0.016
	SMC	0.54 [0.43 0.65]	0.57 [0.40 0.70]	0.53	0.2
Longest- path	FMC	0.53 [0.31 0.81]	0.60 [0.43 0.86]	0.57	0.016
	NEG	0.44 [0.29 0.68]	0.59 [0.37 0.76]	0.60	0.0015
	SMC	0.52 [0.34 0.72]	0.55 [0.36 0.75]	0.52	0.22
Shortest-path	FMC	0.48 [0.22 0.92]	0.45 [0.33 0.67]	0.50	0.47
	NEG	0.37 [0.15 0.71]	0.59 [0.27 0.86]	0.65	7.2x10 ⁻⁵
	SMC	0.40 [0.26 0.60]	0.43 [0.28 0.68]	0.54	0.097
SPD-Count	-	0.069 [0 0.35]	0.15 [0.037 0.40]	0.60	0.0013
SPD-SD	-	0.18 [0.12 0.24]	0.26 [0.19 0.30]	0.68	6.3x10 ⁻⁹
SPD-Area	-	0.13 [0.10 0.18]	0.18 [0.15 0.24]	0.73	1.1x10 ⁻¹²

Table 4. SD across chunks for spatial features

¹ Median [IQR].² Based on 25-spike chunks.³ A_w ranges from 0.5 (no difference) to 1 (non-overlapping distributions).⁴ Mann-Whitney *U*-test.

Figure legends

Figure 1. Pyramidal cells (PYR) and parvalbumin-immunoreactive (PV) interneurons are tagged in freely-moving mice

A. Optical tagging of PV cells. **a.** Every PV::ChR2 mouse was chronically implanted with a four-fiber/four-shank/32-channel optoelectronic array in the neocortex (nCX). Optical stimuli were applied, in separate sessions, in the nCX and in hippocampal region CA1. Peri-stimulus time histogram of the PV cell (bottom), triggered by the onset of 50 ms light pulses applied on the optical fiber attached to the recording shank ($n=20$; $33 \mu\text{W}$). The unit is tagged as PV due to a robust firing rate increase during light (gray) compared to no-light periods. ***: $p<0.001$, Poisson test. **b.** Wide-band (1-5,000 Hz) recordings from four same-shank channels in CA1. Bottom, Spike trains of a PYR (purple) and the PV cell (green).

B. Connectivity-based tagging. Top, Mean ($\pm\text{SD}$) spike waveforms. For every unit, the channel that exhibits the highest trough-to-peak magnitude is denoted the main channel (boxed). Middle, Auto-correlation histograms (ACH), showing burst spiking activity of the PYR (purple). Bottom, Cross-correlation histogram (CCH; black) between the spikes of the PYR and the optically-tagged PV cell. Gray, monosynaptic window. The CCH is consistent with monosynaptic excitation of the PV cell by the reference unit, tagging the reference unit as excitatory (PYR). ***: $p<0.001$, Poisson test.

C. Tagged dataset. Of the 512 units in the dataset, 411 (80.3%) are PYR, and 449 (87.7%) are from CA1.

Figure 2. Waveform-based and spike-timing features allow near-perfect classification of PYR and PV cells

A. Features extracted from the mean waveform of the main channel. Voltage values were scaled by the absolute value at the maximal negativity, yielding arbitrary units (AU; the example units are the same as in Fig. 1B). **a.** Trough-to-peak-duration (*TTP-duration*) feature, defined as the time between the

1027 maximal negativity and the ensuing maximal positivity **b**. Cumulative distribution function (CDF) of the
1028 *TTP-duration* feature for the entire population (n=411 PYR, n=101 PV cells; no chunking). Here and in all
1029 subsequent CDFs, horizontal lines represent 50%, vertical dashed lines indicate medians, and ***
1030 corresponds to $p < 0.001$, *U*-test. The filled circles represent values corresponding to the examples given
1031 in **a**. The difference between PYR and PV cells indicates longer TTP durations for PYR, compared to PV
1032 cells.

1033 **B**. Waveform-based features allow near-perfect classification. Cross-validated random forest models
1034 were trained using the waveform-based features (n=50 partitions). The chunking method yields
1035 improved classification compared to no chunking. The areas under the receiver operator characteristic
1036 (ROC) curves (AUCs) without chunking (blue) and with 50-spike chunks (orange) are higher than chance
1037 level. ***: $p < 0.001$, Wilcoxon test comparing to chance level, 0.5. Inset, Confusion matrices (no
1038 chunking) based on different decision thresholds (top, 0.1; bottom, 0.9) show variability in prediction,
1039 exemplifying the shortcomings of threshold-dependent metrics.

1040 **C**. Features extracted from spike-timing. High-frequency features derived from single-sided short-term
1041 (0-50 ms) ACHs. **a**. The *Uniform-distance* feature is defined as the average absolute difference between
1042 the single-sided ACH and a straight line (the example units are the same as in **Fig. 1B**). **b**. Cumulative
1043 distribution of the *Uniform-distance* feature for the entire population (no chunking). The larger *Uniform-*
1044 *distance* values for PYR indicate larger deviations from linear recovery for PYR, compared to PV cells.

1045 **D**. Classification based on spike-timing features is not consistently improved by chunking. AUCs were
1046 derived from ROC curves based on n=50 cross-validated random forest models. ROC curves for the test
1047 data without chunking (blue) and with 1,600-spike chunks (orange) with performance above chance
1048 level. All conventions are the same as in **B**.

1049 See also Extended Data **Figures 2-1** and **2-2**.

1050

1051 **Figure 3. Transforming multi-channel spike waveforms to event-based delta-like functions removes**
 1052 **all waveform-based information and allows extracting purely spatial features**

1053 **A.** The event-based delta transformation procedure, illustrated for the first median crossing (FMC)
 1054 event. **a.** The mean waveforms, with delta-like functions marking the FMCs. The transformation replaces
 1055 all voltage values with zeros, except for the event points, which are assigned the same value as the
 1056 trough. In gray are channels for which the magnitude of the TTP is below a predetermined threshold
 1057 (*Materials and Methods*). The main channels are boxed. **b.** Next, waveform-related information that
 1058 might be recovered by combining multiple delta-transformed events is removed. The delta-like
 1059 functions are scaled and centralized (arrowheads), placing the event of the main channel at the
 1060 midpoint (129th sample).

1061 **B.** Left, The scaled waveform of the main channel of all units in the dataset before the transformation,
 1062 sorted for PYR and for PV separately by the time of the trough. Right, The same waveforms after event-
 1063 based delta transformation. The transformation removes nearly all of the variability between units.

1064 **C.** Cross-validated random forest models (n=50; no chunking) were trained using waveform-based
 1065 features extracted from the transformed spikes. The confusion matrix, based on a naive decision
 1066 threshold of 0.5, yields a constant prediction of one class. n.s., $p>0.05$, Wilcoxon test. Numbers in every
 1067 cell denote median [IQR]. Performance was quantified by the threshold-independent AUC. The
 1068 classification yields an AUC of exactly 0.5, corresponding to purely random prediction.

1069 **D.** A time-based feature, *FMC-Time-lag-SD*, derived from the differences between the times of the
 1070 FMC event in different channels. The feature quantifies the temporal dispersion of the event, without
 1071 considering the actual positions of the recording electrodes. **a.** *FMC-Time-lag-SD* is defined as the SD of
 1072 the time differences between the FMC event of the main channel (vertical dotted lines) and the other
 1073 channels. In gray are ignored channels, for which the magnitude of the TTP was below a predetermined
 1074 threshold. **b.** Cumulative distribution of the *FMC-Time-lag-SD* feature for the entire population (411 PYR

1075 and 98 PV cells, no chunking). The smaller *FMC-Time-lag-SD* values of the PYR indicates higher
 1076 spatiotemporal synchrony for PYR, compared to PV cells. All conventions for the CDFs here and in
 1077 subsequent panels are the same as in **Fig. 2A**.

1078 **E.** A graph-based feature, *FMC-Average-weight*, derived from the differences between the FMC event
 1079 time in different channels and the electrode locations. **a.** *FMC-Average-weight* is defined as the average
 1080 edge weight in the event graph. The event graph is a directed graph with vertices representing the
 1081 electrodes, and edges representing the transmission speed based on the timing of the events and the
 1082 location of the electrodes. Only channels that passed the threshold for the magnitude of the TTP were
 1083 considered. **b.** Cumulative distribution of the *FMC-Average-weight* feature (no chunking). The larger
 1084 values for PYR indicate higher transmission rates for PYR, compared to PV cells.

1085 **F.** A value-based feature, *SPD-Count*, derived from spatial dispersion (SPD) of the maximal negativity
 1086 on every channel. **a.** *SPD-Count* is defined as the number of channels that reached at least 50% of the
 1087 maximal negativity of the main channel. **b.** Cumulative distribution of the *SPD-Count* feature (no
 1088 chunking). No consistent difference between the PYR and PV is observed, suggesting similar spatial
 1089 distributions of the scaled maximal negativity ($p>0.05$, *U*-test).

1090 See also Extended Data **Figure 3-1**.

1091

1092 **Figure 4. The variance of spatial features over channels and across chunks is different for PYR and for**
 1093 **PV cells**

1094 **A.** Variance over channels differs between events and cell types. Compared to PYR, PV cells show
 1095 lower spatiotemporal spike synchrony (i.e., higher SD) during FMC. The relation reverses during the NEG
 1096 event. The SD of the second median crossing (SMC) event is not consistently different between PYR and
 1097 PV cells. n.s.: $p>0.05$, ***: $p<0.001$, *U*-test. For both PYR and PV cells, synchrony increases from the FMC

1098 to the NEG, and then decreases during the SMC. Lined *: $p < 0.05$, ***: $p < 0.001$, Kruskal-Wallis test,
1099 corrected for multiple comparisons.

1100 **B.** Variance across chunks differs between cell types. Every dot shows the SD value for a different
1101 spatial feature, based on 25-spike chunks. Of 18 features, 13 (72%) differ in the SD values between the
1102 cell type groups, with the SD being higher for PV cells (black lines: $p < 0.05$, gray lines: $p > 0.05$, U-test).
1103 Comparing the median SDs of the 18 spatial features between the cell type groups, PV cells exhibit
1104 higher SDs compared to PYR. Bars (error bars) represent medians (IQR) of the median feature values for
1105 each cell type. ***: $p < 0.001$, two-tailed Wilcoxon test.

1106 See also Extended Data **Figure 4-1**.

1107

1108 **Figure 5. Features based exclusively on spatial information allow accurate classification of PYR and**
1109 **PV cells**

1110 **A.** Classification based on spatial features is boosted by chunking. AUCs were derived from ROC curves
1111 based on $n=50$ cross-validated random forest models. The AUC increases monotonically when chunk size
1112 is reduced. Every boxplot shows median and interquartile range (IQR), whiskers extend for 1.5 times the
1113 IQR in every direction, a plus indicates an outlier, and notches represent 95% confidence intervals based
1114 on bootstrapping with 1,000 repetitions. The best performance (highest AUC) and largest improvement
1115 compared to no-chunking (∞) is observed for 25-spike chunks. ***: $p < 0.001$, Wilcoxon test.

1116 **B.** Spatial features allow accurate classification. ROC curves for the test data without chunking (blue)
1117 and with 25-spike chunks (orange). The AUCs are higher than chance level. All conventions are the same
1118 as in **Fig. 2B**.

1119 **C.** Feature importance analysis for spatial models with 25-spike chunks. Shapley additive explanations
1120 (SHAP) values were used to assess the individual contribution of each feature to the prediction. The
1121 dotted lines represent chance level importance values, based on models trained with shuffled PYR-PV

labels. The features derived from the FMC event are associated with the highest SHAP values, indicating that synchrony at the initial depolarization phase makes the highest contribution to classification outcome. **: $p < 0.01$, ***: $p < 0.001$, one-tailed U -test.

See also Extended Data **Figure 5-1**.

Figure 6. Spatial models generalize poorer than waveform models but better than spike-timing models

A. Cross-validated random forest models ($n=50$) were trained for every modality on the CA1 (left, red) or neocortex (nCX; right, gray) data, and tested separately on different data from CA1 and from nCX. Conventions for boxplots here and in **B** are the same as in **Fig. 5A**. All models exhibit above-chance performance. ***: $p < 0.001$, Wilcoxon test. The performance of models on the non-trained-upon region is highest for waveform-based models and lowest for spike-timing models. **: $p < 0.01$; ***: $p < 0.001$, Kruskal-Wallis test corrected for multiple comparisons.

B. The decrease in performance upon generalization. Generalization error is defined here as the difference between the AUC on the test set of the training region and the AUC on the test set of the non-trained-upon region, divided by AUC on the test set of the training region. Spatial models trained on either region, and spike-timing models trained on CA1 data, show generalization errors larger than zero. n.s.: $p > 0.05$; **: $p < 0.01$; ***: $p < 0.001$, Wilcoxon test. The dashed horizontal line represents the zero-mark, i.e., same performance on CA1 and nCX. When trained on CA1 data (red), spatial models generalize poorer than waveform models but better than spike-timing models. n.s.: $p > 0.05$; *: $p < 0.05$; ***: $p < 0.001$, Kruskal-Wallis test corrected for multiple comparisons.

See also Extended Data **Figures 6-1 and 6-2**.

Extended data figure legends

Extended Data Figure 2-1

Extended Data for Figure 2. Waveform-based feature interrelations

A. Rank (Spearman's) correlations between waveform-based features, grouped by families. Most correlations (26/28; 93%) differ from zero. Blank: $p > 0.05$; *: $p < 0.05$; **: $p < 0.01$; ***: $p < 0.001$, permutation test.

B. Mutual information (MI) between waveform-based features. All pairs (28/28; 100%) exhibit MI values that are higher than chance level. ***: $p < 0.001$, permutation test. Inset, Scatter plot of the MI values between pairs of features and the pairwise absolute rank correlation coefficients (CC) from panel A with statistics for rank (Spearman's) correlation.

Extended Data Figure 2-2

Extended Data for Figure 2. Spike-timing feature interrelations

A. Rank correlations between the spike-timing features grouped by families. Most correlations (27/28; 96%) differ from zero. All conventions here and in **B** are the same as in Extended Data Fig. 2-1.

B. MI between spike-timing features. All pairs (28/28; 100%) exhibit MI values that are higher than chance level. Inset, Scatter plot of the MI between pairs of features and the CCs from panel A.

Extended Data Figure 3-1

Extended Data for Figure 3. Spatial feature interrelations

A. Correlations between the spatial features, grouped by families. 80% (122/153) of the feature pairs exhibit correlations that differ from zero. All conventions here and in **B** are the same as in Extended Data Fig. 2-1.

1167 **B.** MI between spatial features. Most pairs (126/153; 82%) exhibit MI values that are higher than
 1168 chance level. Inset, Scatter plot of the MI and the absolute CCs from panel **A**.

1169

1170 **Extended Data Figure 4-1**

1171 **Extended Data for Figure 4. Time-lag-SS and Shortest-path features across events and cell types**

1172 **A.** *Time-lag-SS* features differ between events and cell types. Compared to PYR, PV cells show larger
 1173 feature values during FMC. The relation reverses during the NEG event. The values during the SMC event
 1174 are not consistently different between PYR and PV cells. For PV cells, feature values decrease from the
 1175 FMC to the NEG, and then increase during the SMC. For PYR, feature values increase between FMC and
 1176 SMC and between NEG and SMC. Here and in **B**, all conventions are the same as in **Fig. 4A**.

1177 **B.** The graph-based *Shortest-path* feature differs between events and cell types. Compared to PYR, PV
 1178 cells exhibit smaller feature values during FMC. The relation reverses during the NEG event. The values
 1179 during the SMC event are not consistently different between PYR and PV cells. For PV cells, feature
 1180 values increase from the FMC to the NEG, and then decrease during the SMC. For PYR, feature values
 1181 decrease between FMC and SMC and between NEG and SMC.

1182

1183 **Extended Data Figure 5-1**

1184 **Extended Data for Figure 5. Distribution of the six most important spatial features**

1185 **A.** Cumulative distributions of the *FMC-Time-lag-SS* feature calculated without chunking. Here and in
 1186 all subsequent CDFs, horizontal lines represent 50%, vertical dashed lines indicate medians. n.s.: $p > 0.05$;
 1187 ***: $p < 0.001$, *U*-test.

1188 **B.** Cumulative distributions of the *FMC-Time-lag-SD* feature.

1189 **C.** Cumulative distributions of the *FMC-Shortest-path* feature.

1190 **D.** Cumulative distributions of the *SMC-Time-lag-SD* feature.

1191 E. Cumulative distributions of the *SMC-Time-lag-SS* feature.

1192 F. Cumulative distributions of the *FMC-Average-weight* feature.

1193

1194 **Extended Data Figure 6-1**

1195 **Extended Data for Figure 6. Models of all modalities generalize between brain regions**

1196 **A.** Models based on waveform-based features (50-spike chunks) were trained on CA1 data (top) or on
1197 neocortical data (bottom). The AUCs were calculated based on $n=50$ models. Performance of waveform-
1198 based models is above chance level when tested on either CA1 (left) or neocortical (right) samples. Here
1199 and **B** and **C**, ***: $p<0.001$, Wilcoxon test.

1200 **B.** Models based on spike-timing features (1,600-spike chunks) were trained on CA1 data (top) or on
1201 neocortical data (bottom). Performance of spike-timing models is above chance level when tested on
1202 either CA1 or neocortical samples.

1203 **C.** Models based on spatial features (25-spike chunks) were trained on CA1 data (top) or on neocortical
1204 data (bottom). Performance of spatial models is above chance level when tested on either CA1 or
1205 neocortical samples.

1206

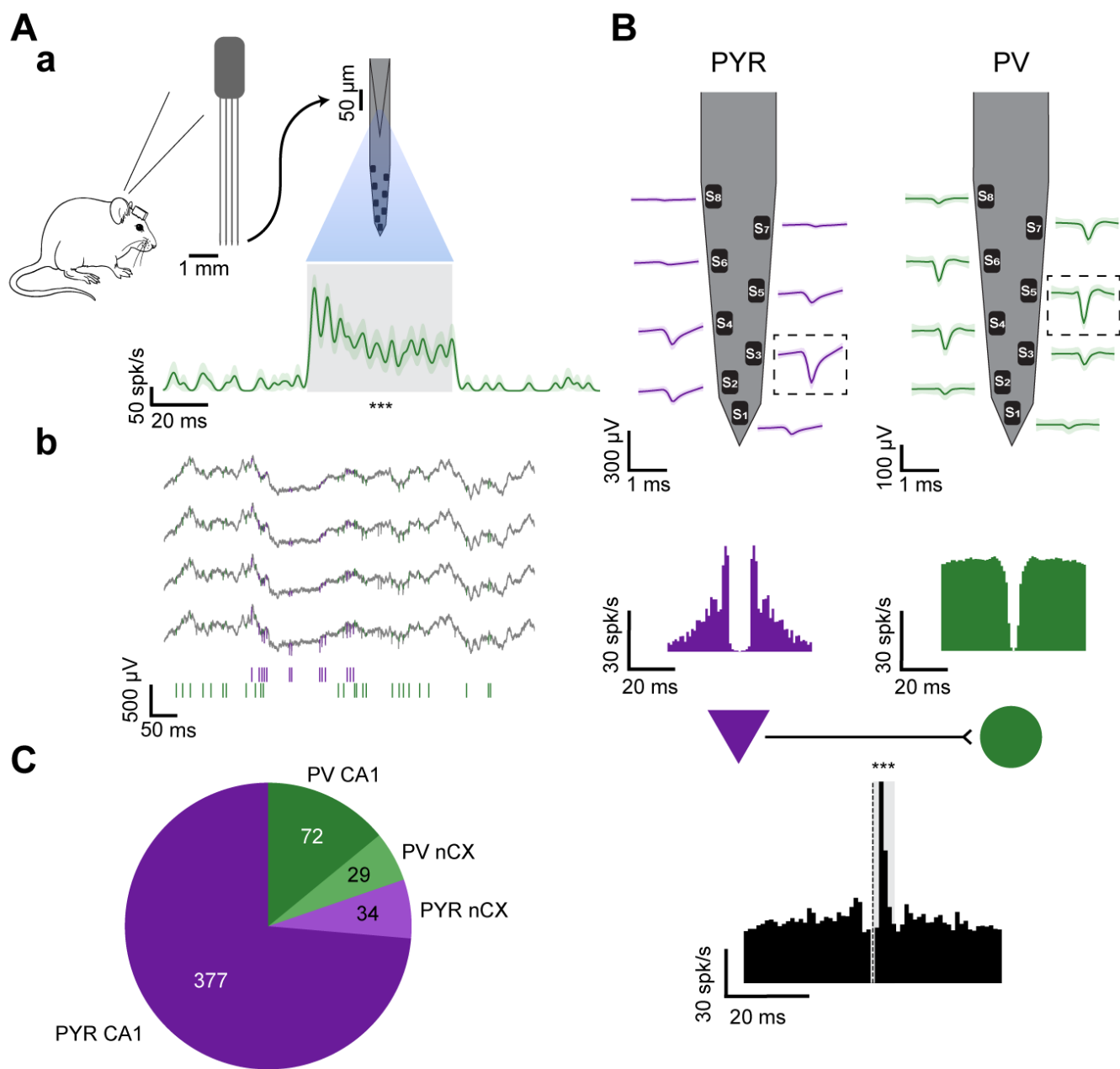
1207 **Extended Data Figure 6-2**

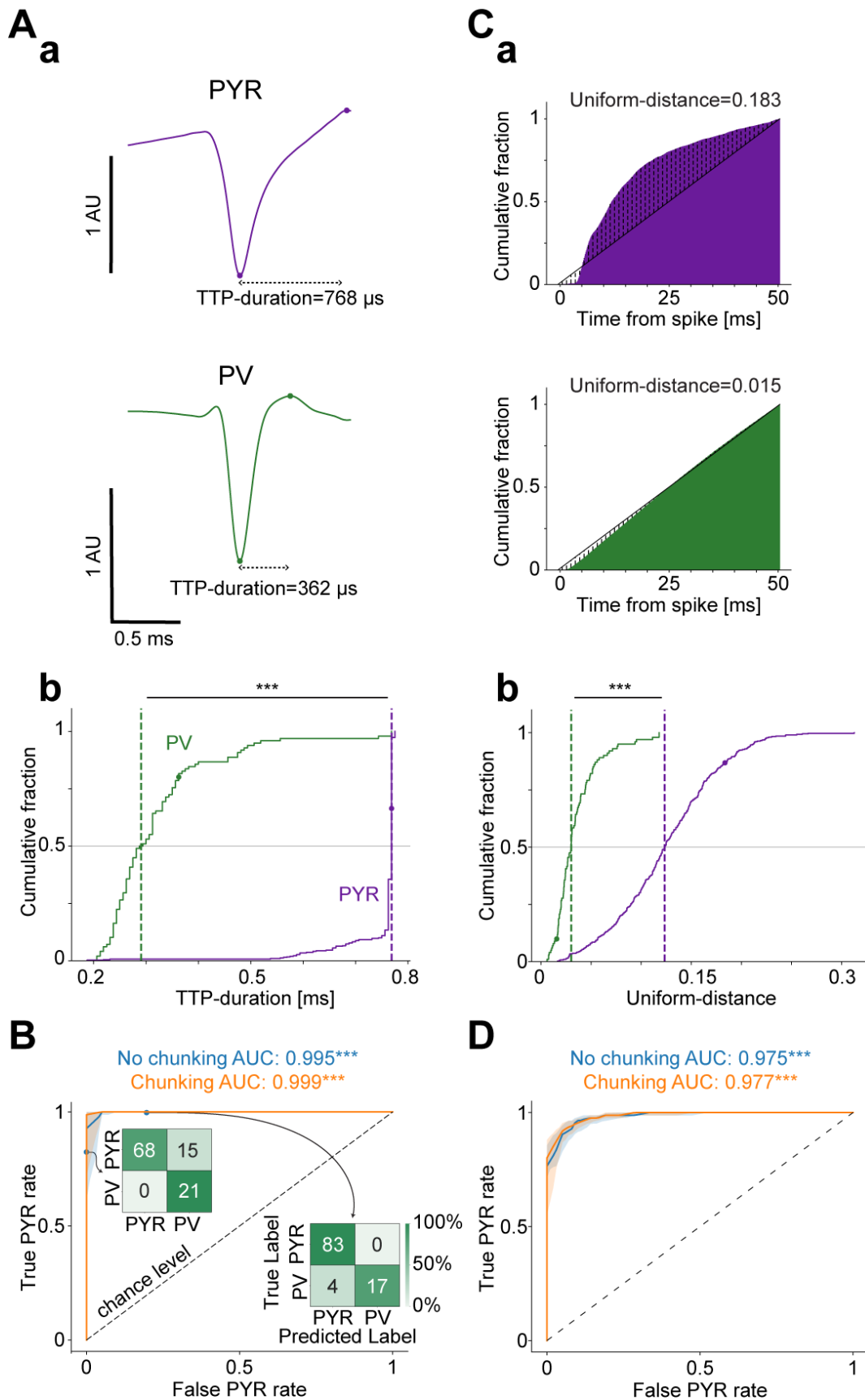
1208 **Extended Data for Figure 6. Spatial feature importance indicates consistent characteristics across** 1209 **regions**

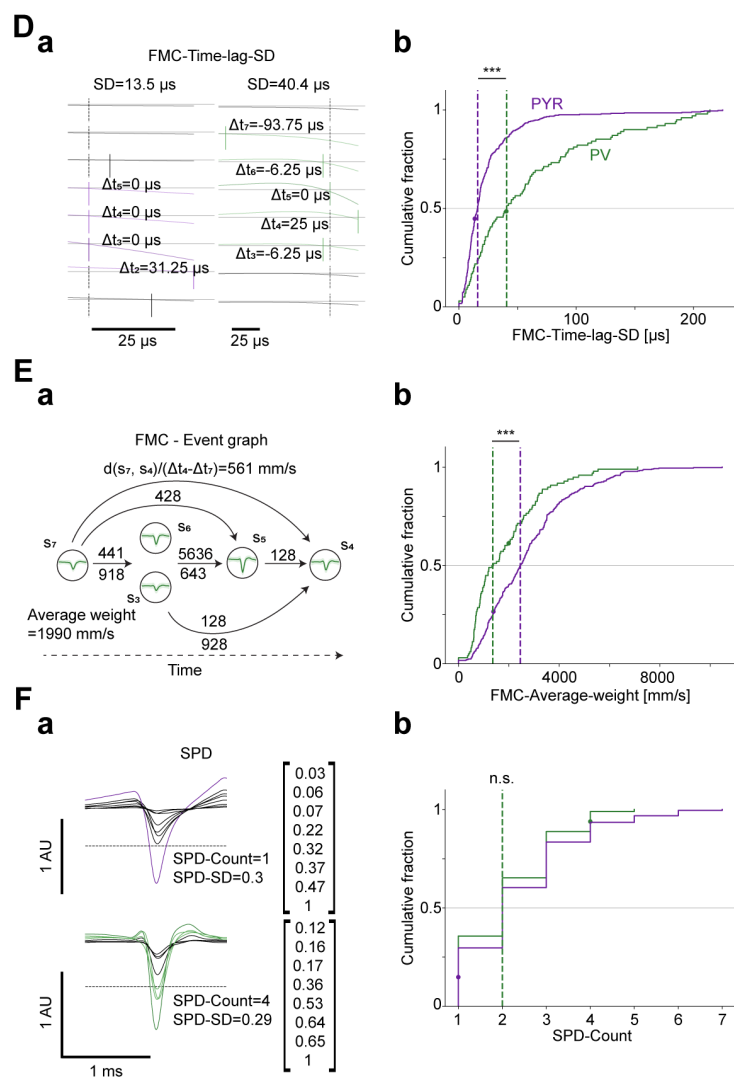
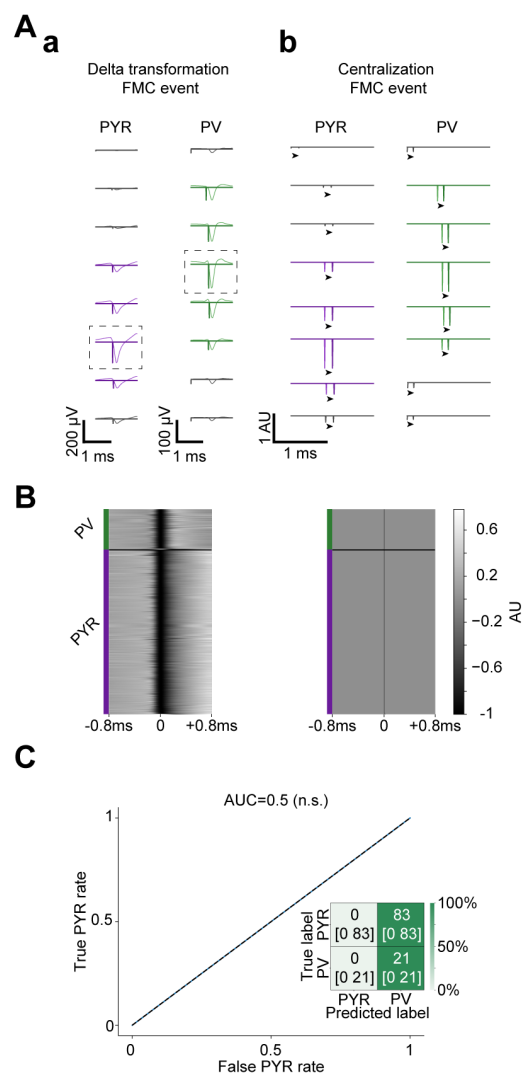
1210 **A.** SHAP values for the spatial models with 25-spike chunks trained only on CA1 data. The six most
1211 important features are the same as the six most important features in the analyses of models trained on
1212 the data from both regions (**Fig. 5C**).

1213 **B.** SHAP values for the spatial models with 25-spike chunks trained on nCX data. The SMC features are
1214 the strongest determinants of the predictions for neocortical-trained models. The six most important

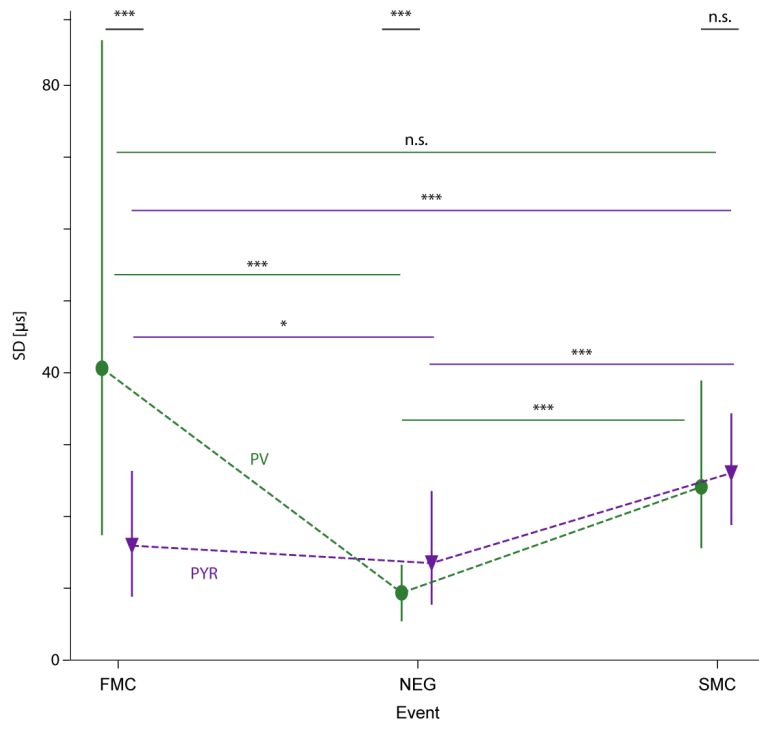
1215 features are the same as for the CA1-trained data (panel **A**) and as for the models trained on the data
1216 from both regions (**Fig. 5C**).







A



B

